

1 **Integrated multi-omics single cell atlas of the human retina**

2

3 Jin Li^{1,2,*}, Jun Wang^{1,2,*}, Ignacio L Ibarra^{3,*}, Xuesen Cheng^{1,2,*}, Malte D Luecken^{3,4}, Jiaxiong
4 Lu^{1,2,5}, Aboozar Monavarfeshani⁶, Wenjun Yan⁶, Yiqiao Zheng⁷, Zhen Zuo¹, Samantha Lynn
5 Zayas Colborn⁸, Berenice Sarahi Cortez⁸, Leah A Owen⁹, Nicholas M Tran¹, Karthik Shekhar¹⁰,
6 Joshua R Sanes⁶, J Timothy Stout¹¹, Shiming Chen^{7,12}, Yumei Li^{1,2}, Margaret M DeAngelis¹³,
7 Fabian J Theis³, Rui Chen^{1,2,5}

8

9 1. Department of Molecular and Human Genetics, Baylor College of Medicine, Houston, Texas,
10 United States.

11 2. Human Genome Sequencing Center, Baylor College of Medicine, Houston, Texas, United
12 States.

13 3. Institute of Computational Biology, Helmholtz Zentrum München, German Research Center
14 for Environmental Health, Neuherberg, Germany.

15 4. Institute of Lung Health & Immunity, Helmholtz Munich; Member of the German Center for
16 Lung Research (DZL), Munich, Germany.

17 5. Department of Biochemistry and Molecular Biology, Baylor College of Medicine, Houston,
18 Texas, United States.

19 6. Center for Brain Science and Department of Molecular and Cellular Biology, Harvard
20 University, Cambridge, United States.

21 7. Department of Ophthalmology and Visual Sciences, Washington University in St Louis,
22 Saint Louis, Missouri, United States.

23 8. Lions Eye Bank of Texas, Baylor College of Medicine, Houston, Texas, United States.

24 9. John A. Moran Eye Center, Department of Ophthalmology and Visual Sciences, University
25 of Utah, Salt Lake City, Utah, United States.

26 10. Department of Chemical and Biomolecular Engineering; Helen Wills Neuroscience
27 Institute; Center for Computational Biology; California Institute for Quantitative Biosciences,
28 QB3, University of California, Berkeley, Berkeley, California, United States.

29 11. Department of Ophthalmology, Cullen Eye Institute, Baylor College of Medicine, Houston,
30 Texas, United States.

31 12. Department of Developmental Biology, Washington University in St Louis, Saint Louis,
32 Missouri, United States.

33 13. Department of Ophthalmology, Ross Eye Institute, Jacobs School of Medicine and
34 Biomedical Sciences, State University of New York at Buffalo, Buffalo, New York, United
35 States.

36

37 *These authors contributed equally to this work.

38 Corresponding author: Rui Chen (ruichen@bcm.edu), Fabian J Theis

39 (fabian.theis@helmholtz-muenchen.de)

40

41 **Abstract**

42 Single-cell sequencing has revolutionized the scale and resolution of molecular
43 profiling of tissues and organs. Here, we present an integrated multimodal reference atlas of
44 the most accessible portion of the mammalian central nervous system, the retina. We
45 compiled around 2.4 million cells from 55 donors, including 1.4 million unpublished data points,
46 to create a comprehensive human retina cell atlas (HRCA) of transcriptome and chromatin
47 accessibility, unveiling over 110 types. Engaging the retina community, we annotated each
48 cluster, refined the Cell Ontology for the retina, identified distinct marker genes, and
49 characterized cis-regulatory elements and gene regulatory networks (GRNs) for these cell
50 types. Our analysis uncovered intriguing differences in transcriptome, chromatin, and GRNs
51 across cell types. In addition, we modeled changes in gene expression and chromatin
52 openness across gender and age. This integrated atlas also enabled the fine-mapping of
53 GWAS and eQTL variants. Accessible through interactive browsers, this multimodal cross-
54 donor and cross-lab HRCA, can facilitate a better understanding of retinal function and
55 pathology.

56

57 **Introduction**

58 The advent of high-throughput single-cell transcriptome technologies has greatly
59 enhanced our exploration of cellular diversity. In particular, it enables the creation of
60 comprehensive atlases for healthy tissues, which are crucial for investigating cellular function
61 and disease mechanisms. In pursuit of these goals, the Human Cell Atlas project (HCA) has
62 coordinated collaborative initiatives to catalog cell types throughout the entire human body^{1,2}.
63 Atlases released to date include the Human Lung Cell Atlas³ and the Human Breast Cell Atlas
64⁴.

65 Within the HCA initiative, the Eye Biological Network aims to create a cell atlas for the
66 human eye. Recent studies have generated atlases of the anterior and posterior segments of
67 the human eye^{5,6}. Other studies have generated retinal atlases from multiple species,
68 including mouse, chick, macaque, and human⁷⁻¹⁵. The goal of the work reported here is to
69 augment previous datasets with additional donors, cells, and methods to generate the first
70 version of a comprehensive cell atlas of the human retina. In the future, we plan to expand
71 this effort to encompass the entire eye.

72 In addition to transcriptomic profiling, the advent of advanced technologies enables the
73 exploration of individual cells in various modalities, such as the Assay for Transposase-
74 Accessible Chromatin with sequencing (ATAC-seq)¹⁶. Such large-scale multimodal datasets
75 are crucial in the construction of reference cell atlases as they are essential for identifying rare
76 cell types and understanding mechanisms previously restricted by individual datasets and
77 single modality profiling. Additionally, examining the effects of donor traits on each cell type,
78 e.g., aging, ancestry, and gender, requires a diverse and substantial set of donor samples.
79 However, integrating extensive datasets is computationally challenging, especially with large
80 and complex data^{17,18}. Consequently, the convergence of substantial data resources, cross-
81 donor investigations, and computational prowess represents an essential paradigm for
82 advancing our comprehension of intricate biological systems and diseases.

83 This study created a comprehensive multi-omics human retina cell atlas (HRCA)
84 through an integrated analysis of over 2 million snRNA-seq nuclei or cells and over 370,000
85 snATAC nuclei. The HRCA encompasses over 110 distinct retinal cell types, achieving nearly
86 complete molecular characterization and comprehensive chromatin accessibility. The
87 inclusion of a diverse set of donors revealed molecular changes during aging and between
88 genders at a cellular resolution, shedding light on potential links to diseases. The chromatin
89 profiles enabled an in-depth exploration of regulons and regulatory mechanisms governing
90 cell classes, subclasses, and cell types in the human retina. Furthermore, this integrated atlas
91 facilitated fine-mapping of causal variants, targeted genes, and regulatory mechanisms

92 underlying GWAS and eQTL variants for retinal cell types. Overall, the HRCA provides a
93 valuable resource for both basic and translational research on the retina.

94

95 **Results**

96 **Single cell atlas of the human retina**

97 To obtain a comprehensive atlas of cell types in the human retina, we integrated seven
98 publicly available datasets ^{7,15,19-23} with newly generated unpublished data (Fig. 1A-B). The
99 integrated dataset totals 2,070,663 single nuclei from 144 samples taken from 52 donors
100 (Supplementary Table 1, 2 and 3). Recovered cells included astrocytes, amacrine cells (AC),
101 bipolar cells (BC), cones, horizontal cells (HC), Müller glia cells (MG), microglia, retinal
102 ganglion cells (RGC), retinal pigment epithelium (RPE), and rods. Annotation of the major
103 classes was performed on individual samples by a coarse label prediction method (Methods).
104 To accommodate the large number of cells, data integration for all cells was employed to
105 facilitate lineage-specific annotations for BC, AC, and RGC, given their complex cell types.
106 The major classes were consistently distributed, except for enriched AC and RGC in several
107 donors from new samples where cell enrichments are performed to increase the proportion of
108 highly heterogeneous classes (AC, BC, and RGC), enabling the annotation of rare cell types
109 (Extended Data Fig. 1A-B and Supplementary Table 4).

110 To facilitate the integrated analysis, an scIB approach ¹⁷ was utilized for benchmarking
111 data integration algorithms, and scVI ²⁴ was selected for the construction of the retinal atlas
112 (Fig. 1C, Methods and Supplementary Note). Using scVI, we integrated the entire 2 million
113 cells and embedded them in 2D using UMAP (Extended Data Fig. 1C). We compared the
114 distribution of scRNA-seq and snRNA-seq within this UMAP and found significant differences
115 between snRNA-seq and scRNA-seq transcriptomic signatures, precluding their alignment
116 using scVI (Extended Data Fig. 1C-D). We also benchmarked the conservation of cell type
117 variation when integrating both data types compared to maintaining separate scRNA-seq and
118 snRNA-seq references (Methods and Supplementary Fig. 1). We observed that combining
119 scRNA-seq and snRNA-seq modalities leads to a less accurate representation of cellular
120 variation (Supplementary Fig. 1C). To compare the transcriptome differences, we visualized
121 the 144 samples by averaging the expressions using pseudo-bulk analysis and confirmed that
122 snRNA-seq and scRNA-seq yield distinct transcriptomes (Extended Data Fig. 1E), consistent
123 with previous reports comparing these sequencing modalities ²⁵. We therefore created two
124 separate references for snRNA-seq (Fig. 1D) and scRNA-seq (Extended Fig. 1F), respectively.
125 Both were verified by the expression of canonical marker genes for each cell class (Extended
126 Fig. 1G).

127 To further investigate the transcriptomic differences between the snRNA-seq and
128 scRNA-seq technologies, cell proportions of major classes were calculated and compared in
129 fovea, macular and periphery regions (Supplementary Fig. 2, Extended Data Fig. 2A and
130 Supplementary Note). The most significant differences in cell proportions observed is that
131 scRNA-seq datasets have a higher proportion of MGs compared to snRNA-seq datasets. Cell
132 clusters from these two technologies can be readily aligned as they share similar
133 transcriptomic signatures of major classes (Fig. 1E). However, a large number of differentially
134 expressed genes (DEGs) were identified between the two technologies (Methods and
135 Supplemental Note). In total, 1,387 and 3,242 over-expressed genes were identified across
136 all cell types in snRNA-seq and scRNA-seq datasets, respectively (\log_2 fold change > 1 , q -
137 value < 0.05) (Fig. 1F and Supplementary Table 5). These over-represented genes exhibited
138 distinct yet biologically related enriched gene ontology (GO) biological processes (Extended
139 Data Fig. 2B-E). For example, genes implicated in biological processes related to
140 ribonucleoprotein complex or ribosome biogenesis, mitochondrial gene expression, and ATP
141 synthesis were enriched in scRNA-seq datasets.

142

143 **Bipolar cells**

144 Over 422,000 bipolar single nuclei included in the current atlas can be divided into 14
145 cell types based on marker genes^{7,9} (Fig. 2A). One significant difference from previous reports
146 is that the giant bipolar (GB) and blue bipolar (BB) are separated into two distinct clusters,
147 primarily due to a significant increase in the cell number (Fig. 2B). To facilitate the annotation
148 of BC clusters, we conducted a cross-species analysis to align human BC clusters with mouse
149 and macaque BC types, leveraging both single-cell transcriptomes and protein sequence
150 embeddings with SATURN²⁶ (Fig. 2C-D). High concordance with one-to-one mapping was
151 observed among the three species, consistent with the previous report^{7,9}. Based on the co-
152 embedding, the human cluster mapped with mouse cell type BC9 is annotated as the BB as
153 BC9 has been reported to exclusively contact S-cones⁹, also known as “blue” cones in humans
154 and macaques¹², while the human cluster mapped with BC8 is annotated as GB. Despite high
155 similarity between GB and BB, 341 genes highly expressed in GB cells, and 887 genes highly
156 expressed in BB cells were identified (Extended Data Fig. 3D, Supplementary Table 6,
157 Supplementary Fig. 3A-B, and Supplementary Note). Among them, *AGBL1* and *SORCS3*
158 showed high specificity for the GB and BB cells, respectively (Fig. 2A, Extended Data Fig. 3B,
159 and Supplementary Fig. 3C). Consistently, 14 BC corresponding clusters were also observed
160 from the scRNA-seq dataset (Supplementary Table 1 and Extended Data Fig. 3A-C).
161 Furthermore, DEGs in GB and BB, including *AGBL1* and *SORCS3*, were confirmed by the

162 scRNA-seq (*p*-value<10⁻⁶), showing a 58% overlap in GB and a 12% overlap in BB (Fig. 2A
163 and E, Extended Data Fig. 3B, Supplementary Fig. 3C, and Supplementary Table 7).

164 In mice, four BC5 types have been identified: BC5A, BC5B, BC5C, and BC5D ¹².
165 However, how these four closely related BC types correlate with BCs in primates has not been
166 fully resolved. Previously, only BC5A in mice exhibited a confident mapping to DB4 in
167 macaques ⁹. As shown in Fig. 2F, two human BC types, DB4a and DB4b, are closely related
168 to BC5A in mice and DB4 in macaques, while BC5B and BC5C in mice appeared most similar
169 to human and macaque DB5. However, the mouse BC5D appears to be an outlier without
170 closely related BC type in primate. To distinguish the BC types, we identified a set of 55 gene
171 markers that shows robust performance (Extended Data Fig. 3E, Supplementary Table 8 and
172 Supplementary Note).

173

174 **Amacrine and retinal ganglion cells**

175 A total of 73 AC types was identified among over 380,000 AC nuclei (Fig. 3A, Extended
176 Data Fig. 4A-B, and Supplementary Table 9), nearly doubling the number of types in a
177 previous study ⁷. Two AC pan-markers, *PAX6* and *TFAP2B*, were confirmed to be highly
178 expressed in these 73 types (Extended Data Fig. 4A). By utilizing markers for GABAergic ACs
179 (the GABA-synthetic enzymes *GAD1* and *GAD2*) ¹⁵ and Glycinergic ACs (the glycine
180 transporter *SLC6A9*), we identified 55 GABAergic AC types, accounting for ~65% of ACs, and
181 11 Glycinergic AC types, accounting for ~23% of ACs. Seven clusters expressed both markers,
182 classifying them as the “Both” AC types, as previously described in mice ¹⁴. Based on
183 expression of additional previously characterized markers ^{9,15,27}, 14 of the 73 AC clusters could
184 be annotated as known AC types (Extended Data Fig. 4C-D, Supplementary Fig. 4A and
185 Supplementary Note). For example, two clusters (HAC10, HAC26) were annotated as
186 Starburst AC (SAC) by *CHAT* and ON-SAC/OFF-SAC by *MEGF10* and *TENM3*, respectively.
187 A set of gene markers to distinguish these 73 AC clusters are identified (Fig. 3B and
188 Supplementary Table 8). To further annotate AC types, a cross-mapping approach was
189 utilized to map the identified AC types with external sources with an existing labeling from
190 public datasets and other species such as macaques and mice (Extended Data Fig. 5A-C,
191 Supplementary Table 9, Supplementary Fig. 5A-C, and Supplementary Note). As expected,
192 high concordance between snRNA-seq and scRNA-seq is observed: 92% (23/25) scRNA-seq
193 clusters can be mapped to this dataset ¹⁵. Similarly, 94% (32/34) macaque AC types ⁹ mapped
194 to the human dataset. In contrast, only 83% (52/63) mouse AC types mapped to humans ¹⁴,
195 including four non-GABAergic non-Glycinergic (nGnG) types in mice ^{14,15} to human clusters (3
196 Glycinergic and 1 GABAergic) (Supplementary Table 9). Eight human clusters (5 GABAergic

197 and 3 Both) do not have a clear correspondence to previously annotated types. All of these
198 clusters appear to be rare cell types, with the most abundant of them comprising only 0.18%
199 of the AC population (670 nuclei).

200 We identified 15 RGC clusters are identified from over 99,000 RGC nuclei included in
201 the atlas (Fig. 3C and Supplementary Table 9). Utilizing previously characterized markers from
202 macaque, five clusters can be annotated (Extended Data Fig. 6A), OFF midget RGC
203 (MG_OFF) by *TBR1* (HRGC1), ON midget RGC (MG_ON) by *TPBG* (HRGC2), OFF parasol
204 RGC (PG_OFF) by *FABP4* (HRGC6), ON parasol RGC (PG_ON) by *CHRNA2* (HRGC7), and
205 an intrinsically photosensitive RGC (ipRGC) by *OPN4* (HRGC10). Consistent with previous
206 findings, the distribution of RGC types in human is highly skewed, with midgets accounting for
207 87.9% of all RGCs. Parasol RGCs, which accounts for 1.8%, are relatively low compared to
208 previous reports^{9,15} due to experimental enrichments (Extended Data Fig. 6B). Cross-species
209 comparisons among humans, macaques and mice reveal that RGC types are highly divergent
210 (Fig. 3D and Extended Data Fig. 6C-D, Supplementary Fig. 6A-C, Supplementary Table 9,
211 and Supplementary Note). As primate RGC types (approximately 18 types)²⁸ are significantly
212 less diverse compared to mouse RGCs (45 molecularly distinct types)¹³, making it challenging
213 to perform cell cluster mapping between humans and mice (Supplementary Table 9 and
214 Extended Data Fig. 6D). Lastly, a set of novel markers for RGC clusters are identified using
215 the binary classification approach (Fig. 3E and Supplementary Table 8).

216

217 **HRCA: chromatin accessibility landscape**

218 To decipher the gene regulatory programs for retinal cell types, 372,967 snATAC
219 nuclei from 52 samples of 26 donors were profiled (Supplementary Table 10 and 11). These
220 nuclei were classified into six neuronal and three glial classes (Fig. 4A-B). Expression of
221 genome-wide genes including canonical marker genes was highly correlated with local
222 chromatin accessibility and inferred gene activity in all cell classes (Fig. 4C, Extended Data
223 Fig. 7A).

224 Based on this dataset, 670,736 open chromatin regions (OCRs) were identified, with
225 70,909 to 237,748 OCRs per cell class (Fig. 4D, Supplementary Table 12). To evaluate the
226 quality of these OCRs, we compared them with the OCRs detected by retinal bulk ATAC-seq.
227 The snATAC-seq OCRs captured most (77.7%) of OCRs detected by bulk ATAC-seq. More
228 importantly, many cell class-specific OCRs absent from bulk ATAC-seq analysis were present
229 in the snATAC dataset, resulting in a three-fold increase in the total number of OCRs (Fig. 4E-
230 F). Although many OCRs are shared among multiple cell classes, 4.14% to 24.4% (9,361 to
231 24,338) of the OCRs per cell class showed differential accessibility depending on cell classes,

232 suggesting potential roles in cell class-specific gene regulation; we refer to these OCRs as
233 differentially accessible regions (DARs) (Extended Data Fig. 7B-C). By calculating the
234 correlation between gene expression or promoter accessibility and chromatin accessibility of
235 surrounding OCRs (-/+250kb), 162,481 linked OCR-gene pairs were identified (Fig. 4G).
236 These linked OCRs are candidate cis regulatory elements (CREs) and the linked genes are
237 likely to be the targets of the CREs. To further validate these putative CREs, particularly those
238 potentially associated with human disease, we conducted massively parallel reporter assays
239 (MPRAs)^{29,30} on 1,820 CREs that were linked to inherited retinal disease (IRD) genes, utilizing
240 the mouse retina as an *ex vivo* system (Methods). Confirming the gene regulation activity of
241 the identified CREs, 27.3% and 6.6% of the CREs displayed strong enhancer and silencer
242 activities, respectively (Fig. 4H, Extended Data Fig. 7D, Supplementary Table 12). In addition,
243 we identified transcription factors (TFs) for major classes by integrating snRNA-seq and
244 snATAC-seq data using SCENIC+³¹ (Fig. 4I, Supplementary Table 13). A significant portion
245 of the identified TFs have been implicated in specification of individual retinal cell classes,
246 such as *OTX2* and *CRX* for photoreceptor cells, *NR2E3* for rods, *RAX2* for cones, *NEUROD4*
247 for BCs, *ONECUT1* and *ONECUT2* for HCs, *TFAP2A* for ACs, and *NFIB* and *LHX2* for MGs
248³²⁻³⁸. Many novel TFs were also identified (Supplementary Table 13).

249 To annotate cell types within classes, we co-embedded snATAC-seq and snRNA-seq
250 data with GLUE and used a logistic regression model to predict the cell type of snATAC-seq
251 cells based on snRNA-seq annotation³⁹ (Methods). For example, 14 BC types corresponding
252 to the 14 cell types by snRNA-seq were identified (Extended Data Fig. 8A-B). Consistently,
253 two snATAC-seq cell clusters were identified for GB/BB and predicted as GB and BB,
254 respectively. Local chromatin accessibility of the marker genes of GB and BB, *UTRN* and
255 *SORCS3* (identified by snRNA-seq, Extended Data Figure 3D-E) also showed high specificity
256 in the corresponding snATAC-seq cell clusters, suggesting gene regulation of *UTRN* and
257 *SORCS3* indeed differ in GB and BB (Extended Data Fig. 8C-D). Similarly, cell types in other
258 heterogenous cell classes, i.e., AC, HC, cone and RGC, as well as non-neuronal cell classes,
259 MG, astrocyte, and microglia cells were distinguished (Extended Data Fig. 8E-H,
260 Supplementary Fig. 7A-B and Supplementary Note).

261

262 The HRCA enables uncovering cell-type-specific gene regulatory circuits

263 To investigate gene regulatory programs governing individual cell types or groups of
264 types (subclasses) within classes, we performed further SCENIC+³¹ analysis (Methods). The
265 identified regulons show high specificity in distinguishing subclasses within the corresponding
266 major cell class, with a maximum regulon specificity score (RSS)³¹ > 0.8 (Extended Fig. 9A-

267 D, Supplementary Table 13, Supplementary Note). Interestingly, these subclass specific
268 regulons are distinct from the regulons that distinguish their respective major cell class. Some
269 subclasses in different classes share the same TFs. For example, *ISL1* specifically regulates
270 ON-BCs within the BC class and the HC1 type within the HC class. Similarly, *NFIX* is specific
271 for ON-BCs within the BC class and Glycinergic-ACs within the AC class. These findings
272 suggest that cell identity is established through a multiple-layered, hierarchical regulation
273 involving combinations of TFs, with individual TFs playing context-dependent roles.

274 Using regulons of individual BC types as an example, a set of high-quality regulons
275 that exhibit strong correlation between expression level of TFs and chromatin accessibility of
276 TF target regions across BC types were identified (Pearson correlation rho > 0.70 or <-0.75,
277 Fig. 5A, Supplementary Table 13). It appears that each cell type is under the control of a
278 combination of activators and repressors. For example, *ISL1* and *SMAD9* are activators, while
279 *MEF2C* serves as both activator and repressor for RBC. Importantly, we identified the
280 regulons potentially governing BB and GB, two closely related BC types discerned in this study.
281 Specifically, *ELK4* and *SALL4* appear as activators for BB and GB, *DMBX1* as both activator
282 and repressor for GB, and *PBX1* as both activator and repressor for BB (Fig. 5A,
283 Supplementary Fig. 8A-B). This aligns with the DEG analysis, where *PBX1* showed
284 significantly higher expression in BB compared to GB ($\log_{2}FC = -1.43$, $p\text{-adjust} = 5.68 \times 10^{-55}$,
285 Supplementary Table 6).

286 It is worth noting that the cell type regulons show reduced cell type specificity
287 compared to those at the cell class and subclass levels, with a maximum RSS lower than 0.5
288 (Extended Data Fig. 9E, Supplementary Table 13). Indeed, we observed potential TF
289 cooperativity, exhibited as overlap of the target regions and target genes among these TFs
290 (Fig. 5B-C, Supplementary Note). For example, a subset of *NFIA* target regions and target
291 genes overlap with those of *MEIS2* and *NEUROG1*, while their target regions are highly
292 accessible and their gene expression level are high in DB3b. Interestingly, *NFIA* target regions
293 and target genes also show overlap with those of *NFIX* and *POU6F2*, while the accessibility
294 of their target regions and their gene expression level are high in DB4b. (Figure 5A-C). Thus,
295 as is the case for classes, the same TF can collaborate with different TFs in distinct types.
296 Consistently, regulon network analysis revealed interconnections among these regulons,
297 demonstrated by the mutual or directional regulation among TFs and their regulation of the
298 shared target regions and target genes (Fig. 5D).

299 To further evaluate the identified TFs, we utilized chromatin accessibility of the target
300 regions of these TFs to predict the cell type via a logistic regression model and a Support
301 Vector Machine (SVM) model (Methods). The logistic regression model achieved a high ROC-

302 AUC value of 0.98 (Figure 5E, Methods), supporting our findings. We also calculated the
303 correlation of regulons based on the regulon activity, which was measured by target region
304 AUC values associated with cell type identities, resulting in 10 regulon modules (Methods, Fig.
305 5F, Supplementary Table 13). Most of these regulon modules have higher AUC values for
306 specific subsets of BC types, particularly those that are more similar in transcriptome profiles
307 (Extended Data Fig. 9F and Fig. 2D, Supplementary Fig. 8C). In summary, these observations
308 suggest that each cell type is defined by a unique TF combination code, established through
309 precise modulation of both TF expression and the chromatin state of their target regions in
310 each type.

311

312 **Differential gene expression associated with age and sex**

313 Differences in retinal functions and disease risks have been associated with individual
314 traits such as age and sex^{40,41}. We sought molecular correlates of these differences in a set
315 of 135 samples from 57 donors (39 male and 18 female) aged 10 to 91 years (Methods and
316 Supplementary Note), including 24 newly profiled samples from 14 young adult donors
317 (Supplementary Table 14, Extended Data Fig. 10A). We identified 465 to 2,693 genes per cell
318 class with age-dependent expression, utilizing a linear mixed effect model (LMM) (*q*-value <
319 0.05, Fig. 6A-B and Extended Data Fig. 10B, Supplementary Table 15, Methods). Notably,
320 surges of gene expression changes were observed around the ages of 30, 60, and 80 across
321 major classes, revealed by a sliding window analysis (Fig. 6C, Supplementary Table 16,
322 Methods). Although the dynamic patterns of gene expression changes were similar across
323 classes, many DEGs (on average 37.6% per cell class) were specific to single classes (Fig.
324 6B, Extended Data Fig. 10C). Gene set enrichment analysis of the age-dependent DEGs
325 pinpointed several pathways activated across cell types (Fig. 6D-E, Supplementary Table 17,
326 FDR < 0.1). They include complement and coagulation cascades, steroid hormone
327 biosynthesis, adaptive immune response, and regulation of calcium ion import (Fig. 6D-E,
328 Supplementary Table 17). Complement pathways have been shown to play important roles in
329 the pathogenesis of age-related macular degeneration (AMD)⁴²⁻⁴⁷, and alterations in steroid
330 hormone homeostasis have been linked to glaucoma^{48,49}. In contrast, the common
331 suppressed pathways included ribosome, cytoplasmic translation, mitochondrial gene
332 expression, and ribonucleoprotein complex assembly, aligning with findings in a fly aging
333 study⁵⁰ (Fig. 6D, Extended Data Fig. 10D). Suppression of oxidative phosphorylation, protein
334 folding and modification process, ATP metabolic process, and several pathways involved in
335 multiple neurodegeneration diseases were observed in RGC (Fig. 6D-E). These results

336 highlight age-related changes in gene expression that may contribute to age-dependent
337 incidence of major retinal diseases.

338 We also observed transcriptomic differences between males and females across cell
339 classes (Supplementary Table 18, Supplementary Note). The majority (87.7%) of DEGs (q -
340 value < 0.05 , $llog2FCI \geq 0.5$) were identified on the autosomes while the remaining (12.3%)
341 were on the X or Y chromosomes. Similar to the DEGs associated with aging, many DEGs
342 between males and females (average 53.6% per cell class) are cell class specific (Fig. 6F)
343 and enriched of both cell type specific and shared GO terms (FDR < 0.1 , Fig. 6G, Extended
344 Data Fig. 10E, Supplementary Table 17, Supplementary Note). For example, immune-related
345 genes such as those involved in cytokine-mediated signaling pathways, viral processes, and
346 innate immune responses are up-regulated in females specifically in MG (Fig. 6G, Extended
347 Data Fig. 10E). This finding aligns with the sexual dimorphism observed in the mammalian
348 immune system, where females have higher levels of immune responsiveness than males^{51,52}
349^{53,54}.

350 Finally, expression of some genes exhibits sex-dependent aging changes driven by
351 sex-age interaction. (Supplementary Table 17 and 19, FDR < 0.1). For examples, genes
352 involved in complement and coagulation cascades, e.g., *A2M* and *F2RL2*, show more
353 significant activation during aging in females compared to males in cones and ACs (Fig. 6H-
354 I). This result aligns with the previous studies suggesting *F2RL2*'s role in progression to
355 advanced macular disease with neovascularization⁵⁵ and higher prevalence of neovascular
356 age-related macular degeneration in females than males⁵⁶. Conversely, genes involved in
357 autophagy exhibit more significant up-regulation over aging in males compared to females in
358 RGCs and ACs (e.g., *ATG4A*, *CTSD*, *PRKCD*, *ULK1* in RGC, Fig. 6H-I). Interestingly,
359 autophagy has been found to play a crucial role in glaucoma^{57,58}, which is more prevalent in
360 males than females^{59,60}.

361

362 **Leveraging the HRCA to study GWAS and eQTL loci**

363 The HRCA provided a unique opportunity to prioritize candidate causal variants, genes,
364 and affected cell types underlying GWAS traits in a multimodal way. To demonstrate this utility,
365 we first identified enriched cell classes associated with GWAS traits based on cell class
366 specific OCRs and gene expression using LDSC⁶¹ and MAGMA⁶², respectively (Fig. 7A,
367 Supplementary Fig. 9A, q -value < 0.05). Consistent results are obtained from both snRNA-
368 seq and snATAC-seq datasets. We observed significant enrichment of age-related macular
369 degeneration (AMD)-associated loci in Retinal Pigment Epithelium (RPE) and Microglia⁶³.
370 Loci linked to the thickness of the outer segment (OST), inner segment (IST), and outer

371 nuclear layer (ONL) exhibited enrichment in rods, cones, and MGs ⁶⁴. Loci associated with
372 traits related to open-angle glaucoma were enriched in MGs and Astrocytes ⁶⁵⁻⁶⁷. Refractive
373 error and myopia loci showed enrichment across most retinal cell classes ⁶⁸. As a negative
374 control, bone mineral density loci did not display enrichment in any of the retinal cell classes
375 ⁶⁹.

376 To further identify candidate causal variants, target genes, and affected cell types for
377 GWAS loci, we performed fine-mapping of GWAS loci associated with seven retinal GWAS
378 traits: OST ⁶⁴, IST ⁶⁴, ONL ⁶⁴, POAG ⁶⁵, AMD ⁶⁸, refraction error/myopia ⁶⁸, and diabetic
379 retinopathy ⁷⁰. Based on summary statistics and linkage disequilibrium of genome-wide
380 variants analyzed in previous GWAS studies, we identified 18,959 variants that fell within the
381 95% credible sets of these GWAS loci (Fig. 7B and Supplementary Table 20). Notably, a
382 substantial proportion (19.4%, n=3,673) of the variants were found within OCRs (i.e., snATAC-
383 seq peaks). Additionally, small subsets of variants were mapped in regions where target genes
384 could be inferred: 4.2% (796) were within linked CREs, 3.1% (592) within promoter regions,
385 and 2.9% (553) within exonic, 3' UTR and/or 5' UTR regions, resulting in 1,784 variants linked
386 to 691 potential target genes (Table 1). By cross-referencing these GWAS variant-gene pairs
387 with eQTL-eGene pairs identified in bulk retina tissue, we found that 130 GWAS genes were
388 eGenes of the GWAS variants, reinforcing the validity of our findings. Furthermore, a
389 significant proportion of the identified target genes are marker genes of disease relevant cell
390 classes, known genes linked to complex diseases or inherited retinal diseases (Table 1).
391 Specifically, we uncovered well-known AMD related genes such as *APOE*, *C2*, and *C3*. In the
392 case of POAG, our findings included *EFEMP1* ⁷¹, which has been linked to familial juvenile-
393 onset open-angle glaucoma, as well as *TMCO1* and *SIX6*, known to be associated with POAG
394 ⁷². For diabetic retinopathy, *ABCF1* was identified as a regulator of RPE cell phagocytosis ⁷³
395 and as one of the proteomic biomarkers of retinal inflammation in diabetic retinopathy ⁷⁴. For
396 target genes linked to retinal layer thickness, we pinpointed *ATOH7*, *PAX6*, *VSX2*, and *RAX*,
397 all of which have been implicated in retinogenesis ^{75,76}. Additionally, we identified genes like
398 *MKKS*, *FSCN2*, *PDE6G*, *PRPH2*, *RDH5*, *RHO*, *SAG*, *RP1L1*, and *RLBP1*, known to be
399 associated with inherited retinal diseases. Similarly, we fine-mapped retinal eQTLs using a
400 comparable method (Fig. 7C). A significant portion of eQTL variants was also found within
401 OCRs, while eQTLs exhibited greater enrichment in promoter regions than GWAS variants
402 (two-sided binomial test, $p = 4.94 \times 10^{-324}$, Supplementary Table 21). Moreover, these fine-
403 mapped variants provided candidates to study regulatory mechanism of GWAS loci
404 (Supplementary Note). As an example, one POAG variant (rs3777588) was fine-mapped
405 (posterior inclusion probability [PIP]=0.72) to a LCRE of *CLIC5* (Fig. 7D), a region specifically

406 open in MG. Consistently, *CLIC5* is highly expressed in MG among retinal cell classes.
407 Furthermore, the GWAS signal was colocalized with retinal eQTL signal of *CLIC5* through this
408 variant (H4=1.00 and Methods). Notably, this variant was also predicted to strengthen the binding
409 of the transcription factor *HSF1*.

410

411 Discussion

412 In this study, we introduced HRCA version 1, an integrated multi-omics single-cell atlas
413 of the human retina, which marks the first multi-omics reference atlas in the HCA framework
414 ^{1,2}. The HRCA provides a comprehensive view of the transcriptomic and chromatin profiles of
415 retinal cells, comprising data from more than 2 million sn-/sc-RNA-seq cells and over 370,000
416 snATAC-seq cells. Our cross-donor and cross-lab atlas provides a model for future HCA
417 atlases. The HRCA is accessible for the community through numerous interactive platforms,
418 including CELLxGENE ⁷⁷, UCSC Cell Browser ⁷⁸, and Single Cell Portal ⁷⁹, and can therefore
419 serve as a common reference for advancing research on human eye health and diseases.

420 Given the large number of cells profiled, coupled with targeted cell enrichment, the
421 HRCA is nearly saturated for retinal cell types. The integrated analysis of over 2 million single
422 cell/nuclei, including 1.4 million unpublished data points, revealed over 110 cell types in the
423 human retina, nearly doubling the number reported in previous studies ⁷. For example, the
424 HRCA separates two rare and closely related BC types, GB and BB, which co-clustered in
425 previous analyses ^{7,9,15}. Cross-species comparisons among humans, macaques, and mice
426 augment those reported previously ^{7,9,15}, especially with additional species ⁸, improving cell
427 type annotation and providing guidance for translational studies in rodents of human vision
428 disorders. Further annotation of this atlas by experts from the community will be used to
429 update the HRCA.

430 The HRCA also provides a comprehensive gene regulatory landscape of the human
431 retina at single-cell resolution, uncovering over 670K open chromatin regions, and revealing
432 potential CREs in individual cell type contexts. These results enable the identification of GRNs
433 defining cellular identities at the class, subclass, and cell type levels, revealing a multiple-
434 layered, hierarchical regulation principle involving combinations of TFs. Hundreds of CREs
435 linked to IRD genes were validated through a high-throughput functional assay in an *ex vivo*
436 mouse model system. However, a high proportion of inactive sequences were observed in
437 validation, which may result from a combination of limited experimental sensitivity, divergent
438 human-mouse CRE activity, and inactive or false enhancers. Silencers in scrambled CRE
439 sequences could result from retained motif content but low motif diversity ⁸⁰.

Intriguingly, the HRCA also enabled the discovery of dynamic patterns of transcriptome during aging, where DEG surging patterns were consistent across cell types, but the individual genes were mostly differentially expressed in only one or two cell classes. A subset of aging-related DEGs is overlapped with GWAS genes of aging-related diseases, e.g., C3 in Rod and VEGFA in Cone, and aging-related biological pathways include some known to be associated with age-related diseases, such as age-related macular degeneration. Similarly, we detected cell type specific transcriptomic and pathway difference between sexes beyond sex chromosomes, including immune response-related dimorphisms in autosomal genes expression. Interestingly, certain genes show sex-specific aging patterns, which may shed light on gender differences in certain age-related diseases.

Finally, the HRCA facilitated a comprehensive functional annotation of disease-related variants, and exploration of the regulatory mechanisms of causal variants. By combining HRCA with fine-mapping, we identified potential causal variants, target genes, and the acting cell types associated with GWAS and eQTL loci, providing testable hypotheses about the action mode of GWAS variants. Additionally, we offer utilities designed to automate the annotation of cell types for new samples using scArches⁸¹ (Supplementary Fig. 10 and Supplementary Note). In summary, the HRCA represents a comprehensive reference of the human retina and facilitates future analysis across cell types, individuals, and diseases for the human eye.

459

460 Methods

461 Human retina sample collection

462 Tissues not described in previous publications were obtained from 28 individuals within
463 6 hours post-mortem from the Utah Lions Eye Bank. Detailed donor information can be found
464 in Supplementary Table 2. The procedure for dissecting the eyes followed the established
465 protocol ⁸². Macular samples were collected using disposable biopsy punches measuring 6
466 mm in diameter. Subsequently, the retinal tissues were flash-frozen in liquid nitrogen and
467 stored at -80 °C until nuclei isolation. Only healthy donors with no recorded medical history of
468 retinal diseases were included in this study. Post-mortem phenotyping using OCT was
469 conducted to confirm the absence of disease phenotypes, such as drusen or atrophy, as
470 described in the previous study ⁷. Institutional approval for the patient tissue donation consent
471 was obtained from the University of Utah, adhering to the tenets of the Declaration of Helsinki.
472 Each tissue was de-identified in accordance with HIPAA Privacy Rules.

473

474 Nuclei isolation and sorting

475 The frozen retinal tissues were resuspended and triturated in a freshly prepared, pre-
476 chilled RNase-free lysis buffer (10 mM Tris-HCl, 10 mM NaCl, 3 mM MgCl₂, 0.02% NP40) with
477 a Wheaton™ Dounce Tissue Grinder to obtain nuclei. To enrich the retinal ganglion cell nuclei,
478 isolated macular retinal nuclei were stained with a mouse anti-NeuN monoclonal antibody
479 (1:5000, Alexa Flour 488 Conjugate MAB377X, Millipore, Billerica, Massachusetts, United
480 States) in staining buffer (1% BSA in PBS, 0.2U/μl RNAse inhibitor) for 30 minutes at 4°C.
481 After centrifugation at 500g 4°C for 5 minutes, nuclei were resuspended in staining buffer and
482 filtered with a 40μm Flowmi Cell Strainer. DAPI (4',6-diamidino-2-phenylindole, 10 μg/ml) was
483 added before fluorescent cytometry sorting.

484 The stained nuclei were sorted with a BD (Becton Dickinson, San Jose, CA) Aria II
485 flow sorter (70μm nozzle). Gating was performed based on flow analysis of events and
486 strengths of DAPI (450-nm/40-nm-band pass barrier filter) and FITC (530-nm/30-nm-band
487 pass filter) signals. The sorting rate was 50 events per second based on side scatter (threshold
488 value > 200). The nuclei group with strongest 5% FITC signal was collected for RGC
489 enrichment, specifically, while all DAPI-positive nuclei were collected for general retinal nuclei
490 study.

491 For single nuclei ATAC profiling, nuclei were isolated in fresh-made pre-chilled lysis
492 buffer (10 mM Tris-HCl, 10 mM NaCl, 3 mM MgCl₂, 0.02% NP40, 1% BSA) with a Wheaton™
493 Dounce Tissue Grinder until no tissue pieces were visible. After being washed at 500g, 4C for
494 5min twice in a pre-coated 5ml round bottom Falcon tube (wash buffer: 10 mM Tris-HCl, 10 mM
495 NaCl, 3 mM MgCl₂, 1% BSA; coating buffer: 10 mM Tris-HCl, 10 mM NaCl, 3 mM MgCl₂,
496 4% BSA; Falcon tube Cat. NO. 352054), the nuclei were resuspended in 1X diluted nuclei
497 buffer (10X PN-2000153, PN-2000207) with a final concentration of 3000-5000 nuclei/ul.
498

499 **Single-nuclei RNA and ATAC sequencing**

500 All single-nuclei RNA and single-nuclei ATAC sequencing was conducted at the Single
501 Cell Genomics Core at Baylor College of Medicine in this study. The library preparation and
502 sequencing of single-nuclei cDNA were carried out following the manufacturer's protocols
503 (<https://www.10xgenomics.com>). To obtain single cell GEMS (Gel Beads-In-Emulsions) for
504 the reaction, single-nuclei suspension was loaded onto a Chromium controller. The library for
505 single nuclei RNA-seq was prepared with the Chromium Next GEM Single Cell 3' Kit v3.1 (10x
506 Genomics), while the library of single nuclei ATAC-seq was prepared with the Chromium Next
507 GEM Single Cell ATAC Library and Gel Bead Kit v1.1 (10x Genomics). The constructed
508 libraries were subsequently sequenced on an Illumina Novaseq 6000
509 (<https://www.illumina.com>).

510

511 **Data preprocessing of unpublished and public datasets**

512 Raw sequencing reads were first downloaded for all the curated public datasets. Along
513 with unpublished generated datasets, data samples were processed using the same versions
514 of software and databases by a quality control pipeline (<https://github.com/lijinbio/cellqc>). Raw
515 sequencing reads were first analyzed using 10x Genomics Cell Ranger (version 7.0.1)⁸³
516 utilizing the hg38 genome reference obtained from 10x Genomics
517 (<https://cf.10xgenomics.com/supp/cell-exp/refdata-gex-GRCh38-2020-A.tar.gz>). The
518 resulting feature count matrices were retained for downstream quality control. Cell Ranger
519 implemented EmptyDrops to filter empty droplets in experiments based on significant
520 deviations from a background model of low-count cells⁸⁴. To further eliminate potential empty
521 droplets from the filtered feature count matrices by Cell Ranger, dropkick was utilized to
522 construct dataset-specific training labels by applying a logistic regression for real cells, with a
523 threshold based on the total number of transcript counts in cells⁸⁵. The real cells retained
524 were those identified by both EmptyDrops and dropkick, and they were preserved for
525 downstream analysis. To correct for the background transcript measurements derived from
526 ambient RNAs that are not endogenous to cells, SoupX was used to estimate a global
527 contamination fraction across cells and to correct gene expression profiles by subtracting the
528 contaminations⁸⁶. To exclude potential multiplets, DoubletFinder simulated artificial doublets
529 and ranked real cells based on the proportion of artificial neighbors⁸⁷. Cells predicted to be
530 multiplets with high proportions of artificial neighbors were ruled out. Following cell filtering
531 criteria of ≥ 300 features, ≥ 500 transcript counts, and $\leq 10\%$ (or $\leq 5\%$ for snRNA) of reads
532 mapped to mitochondrial genes, the retained cells constituted the clean cells for downstream
533 analysis.

534 To annotate major retinal cell classes, a pre-trained multi-class classifier was applied
535 using scPred to predict a type for each cell⁸⁸. The training data was constructed in-house by
536 collecting cells with ten major annotated cell classes, including amacrine cells (AC), bipolar
537 cells (BC), horizontal cells (HC), retinal ganglion cells (RGC), retinal pigment epithelium (RPE),
538 astrocytes, muller glia (MG), microglia, rods and cones. Raw gene expression counts were
539 initially log-normalized and scaled using Seurat. The scaled matrix was decomposed through
540 principal component analysis. The principal component embeddings were the features utilized
541 for training binary-SVM classifiers (one-versus-all) for cell types. During prediction, the raw
542 counts matrix of test data was also initially log-normalized and scaled using Seurat^{89,90}. The
543 scaled data were then projected into the principal component coordinate basis established by
544 the training data. The projected principal components served as features for prediction against

545 the trained classifiers. Positive cell types were predicted based on classification probabilities
546 ≥ 0.9 , and doublets were identified if cells were classified into multiple types.

547

548 **Integration benchmarking of single cell and single nuclei RNA-seq sequencing**

549 An integration benchmarking of retina datasets was conducted based on previous work,
550 such as scIB¹⁷ and the Human Lung Cell Atlas v1³. Briefly, cells from each donor and
551 sample were independently annotated using one of nine major class cell types using scPred,
552 and then these datasets were concatenated as a single input object, with annotations for
553 batches, cell types, and technologies (sc or sn). We tested two levels of feature selection,
554 1,000 and 3,000 highly variable genes (HVGs), we only tested raw counts without rescaling
555 based on previous insights.

556 To allow batch correction comparisons between single-cell and single-nuclei datasets,
557 we performed three integration pipelines: one with only single-cell RNA-seq datasets (sc), one
558 with only single-nuclei RNA-seq datasets (sn), and one with both dataset types combined
559 (sn+sc). This allowed measuring the integration quality of cells based on matched cells from
560 the combined technologies, with respect to each technology alone.

561 Due to scaling limitations while running methods for the largest single-cell datasets,
562 (more than two million cells), we limited our tests to Python methods with a scalable
563 implementation. Empirically, methods were discarded if output was not generated in 48 h as
564 a single task, with 150GB of memory, 4 CPUs, and one GPU if required. Based on these
565 criteria, we were able to generate batch-corrected objects for 7 methods using 1,000 HVGs,
566 including scANVI, scVI, scGen, scanorama, BBKNN, Harmony (harmonpy), and combat.
567 When using 3,000 HVGs and sn-datasets, scanorama and BBKNN were discarded. When
568 benchmarking sn+sc datasets, scGen and Combat were discarded due to running times.

569 The calculation of some metrics requires a non-linear time with respect to the number
570 of cells, and this makes their computing expensive for the largest datasets. As an improvement
571 during the metrics calculation step, we incorporated into our pipeline a metrics approach to
572 allow fixed subsamples of the full object, with custom percentage sub-samples set up as 3, 5,
573 and 6 percent. This allows measuring integration quality with a sample representative of the
574 full object, and in a shorter computational time, while recovering best methods with a lower
575 computational effort.

576

577 **Integration of single cell and single nuclei transcriptome data**

578 From the benchmark results, scVI²⁴ outperformed all the label-agnostic methods in our
579 benchmark results. Therefore, scVI was selected for integrating the transcriptome data. On

580 the entire 2 million cells, the major cell classes are well integrated, but the subclass clusters
581 within the major classes are mixed. For example, many clusters of the AC class are intermixed
582 with clusters of the BC class (Extended Data Fig. 1C). We compared the cell distribution of
583 snRNA-seq and scRNA-seq and found that many cell clusters overlap between the two
584 technologies, while a few do not (Extended Data Fig. 1D). Therefore, separate integrations for
585 single-nuclei and single-cell samples were conducted to account for the differences in
586 dissociation technologies. For integrating data specific to BC, AC, and RGC types, only
587 subsets of cell type-specific cells for subclass integration were retained. To capture the
588 nuanced similarities between cell clusters, the top 10,000 highly variable genes were calculated
589 using the “sampleID” as the batch key with the Scanpy Python package ⁹¹. The “sampleID”
590 was also used as the batch variable in the scVI modeling. In scVI, two hidden layers for
591 encoder and decoder neural networks and a 30-dimensional latent space were calculated to
592 represent cells after removing sample batches. The number of epochs was adjusted based
593 on the total number of cells in the subclass integration and a minimum of 20 epochs was used
594 for the variational autoencoder training. The trained latent representation was used to
595 measure the distance among cells. These distances were used to calculate the cell clustering
596 using the Leiden algorithm ⁹². To facilitate the inspection of integrated cell clusters, 2D
597 visualization was generated using UMAP ⁹³. To determine the optimal resolution for the Leiden
598 clustering, a range of resolution values were evaluated and manually examined by the
599 resulting cell clusters using a UMAP plot. To assess and mitigate potential over-clustering, the
600 self-projection accuracy of the clustering was computed using the SCCAF Python package ⁹⁴.
601 Furthermore, a two-level clustering method was used to capture the cellular diversities of BC,
602 AC, and RGC when performing subclass clustering. Various resolutions were tested for
603 clustering, and the first-level resolution was selected to achieve initial clustering without over-
604 clustering, as confirmed by UMAP visualization. In the second-level clustering, various
605 resolutions were also tested to refine any under-clustering and achieve optimal clustering
606 without over-clustering on UMAP. Ultimately, the two-level clustering approach determined
607 the number of clusters in the atlases.

608

609 **Comparison between snRNA-seq and scRNA-seq**

610 To evaluate the differences between snRNA-seq and scRNA-seq, the cell proportions
611 of major cell classes were computed in each sample using both technologies. The samples
612 were categorized into fovea, macular, and periphery tissue regions for both approaches. To
613 address any potential cell proportion bias arising from experimental enrichment in a subset of
614 snRNA-seq samples, only samples without enrichment were included. Subsequently, bar plots

615 were generated to compare the cell proportions of major classes across tissue regions for the
616 two technologies.

617 To examine the cell type similarities of major classes between the two technologies,
618 raw counts of the complete cells were first aggregated into pseudo-bulk for each major class
619 across samples. The resulting pseudo-bulk measurement has three metadata columns: the
620 “sampleID,” which represents unique sample IDs in the atlas; “dataset,” indicating whether the
621 sample is from “snRNA” or “scRNA” technologies; and the “majorclass,” which denotes the
622 annotated major class cell types. Utilizing the pseudo-bulk count matrix, cell type similarities
623 were calculated using the MetaNeighbor R package ⁹⁵. Specifically, highly variable genes
624 were detected using the “variableGenes()” function with “dataset” as the source of samples,
625 and the mean AUROC matrix was calculated for “dataset” and “majorclass” using the
626 “MetaNeighborUS()” function with the calculated variable genes.

627 To identify differentially expressed genes in two technologies, the DESeq2 R package
628 ⁹⁶ was applied to the aggregated pseudo-bulk count matrix. To account for major class cell
629 type information during the statistical test, the design formula used “~ majorclass + dataset”.
630 The Wald test was employed to calculate *p*-values of gene expression differences between
631 the two technologies. The contrast used in the “results()” function was “contrast=c(‘dataset’,
632 ‘snRNA’, ‘scRNA’)” to derive differentially expressed genes after regressing out major classes
633 by “majorclass”. To enhance the statistical power, genes with average expressions less than
634 10 among pseudo-bulk samples were excluded from the analysis. For calculating adjusted *q*-
635 values from the *p*-values, we employed the Benjamini-Hochberg procedure ⁹⁷. Subsequently,
636 differentially expressed genes were identified under \log_2 fold change >1 and *q*-value <0.05 .
637 Enriched Gene Ontology (GO) terms were identified using the “enrichGO()” function of the
638 clusterProfiler R package ⁹⁸ on the differentially expressed genes. To investigate gene
639 expression changes among major class cell types between the two technologies, the count
640 matrix was subsetted per major class and subjected to differential gene expression analysis
641 using the design formula “~ dataset” in a similar manner. To explore the shared differentially
642 expressed genes across major classes, an UpSetR image was produced using the “upset()”
643 function from the UpSetR R package ⁹⁹.

644

645 **Cross-species analysis**

646 To conduct cross-species analysis, the SATURN algorithm²⁶ was utilized to compare
647 human, mouse, and macaque cell clusters and cell types. The human cell clusters were
648 identified from clean cells, while the mouse reference was generated from an integrated
649 analysis of collected mouse samples available at the data portal of Baylor College of Medicine

650 (https://mouseatlas.research.bcm.edu/). Raw single cell measurements and cell labeling for
651 the macaque reference were obtained from the GEO repository (accession GSE118546)⁹. To
652 ensure accurate alignment of cell clusters, we randomly sampled up to 2,000 cells per cell
653 cluster and cell type. Protein embeddings for human, mouse and macaque are retrieved from
654 the respective SATURN repositories. To capture nuanced similarities among cell clusters,
655 SATURN feature aggregation employs a set of 5,000 macrogene. Additionally, during pre-
656 training, “sampleID”s are utilized as non-species batch keys to effectively reduce batch effects
657 caused by samples. The trained 256-dimensional latent representations were utilized to
658 compute cell dissimilarities and generate UMAP for visualizations.

659

660 **Differential gene expression analysis for bipolar cells**

661 The DESeq2 R package⁹⁶ was utilized to identify genes that were highly expressed in
662 specific cell types, e.g., GB and BB cell types. First, a pseudo-bulk measurement was
663 calculated by summing the gene expressions of single cells within each cell type for each
664 sample, excluding samples with less than 2,000 cells. The pseudo-bulk datasets were then
665 used in a paired test, incorporating sample information in the design formula “~ sampleID +
666 celltype”. Lowly expressed genes with an average expression less than 10 were filtered out to
667 improve computation speed and statistical power. A Wald test was used to calculate *p*-values
668 for differential testing, comparing gene expression changes between BB and GB by
669 contrasting the “celltype” factor using the DESeq2 package’s “results()” function. The adjusted
670 *q*-value was calculated from *p*-values using the Benjamini-Hochberg procedure⁹⁷. The
671 EnhancedVolcano R package¹⁰⁰ was used to visualize the distribution of log2 fold change and
672 *q*-values. Differentially expressed genes were identified based on criteria of log2 fold
673 change > 1 and *q*-value < 0.05. Enriched Gene Ontology (GO) terms were identified using the
674 “enrichGO()” function of the clusterProfiler R package⁹⁸ on the changed genes.

675 To identify the top-ranked genes in GB and BB between the snRNA-seq and scRNA-
676 seq datasets, we normalized and transformed raw count matrices from the two technologies
677 using the “normalized_total()” and “log1p()” functions within the Scanpy Python package⁹¹. To
678 expedite the computation, 10,000 highly variable genes were calculated using the “seurat”
679 flavor with the batch key set as the “sampleID”. Subsequently, the highly variable genes were
680 tested for top-ranked genes via the Wilcoxon test. Top-ranked genes were identified by *q*-
681 value < 0.05. To visualize the overlapped genes, a venn diagram was generated using the
682 “venn.diagram()” function from the VennDiagram¹⁰¹ R package. Fisher’s exact test was used
683 to calculate the significance of the overlap of top ranked genes between GB and BB in snRNA-
684 seq and scRNA-seq, with 10,000 genes as the background for gene expression.

685 To evaluate the cell type similarities between DB4a, DB4b, and DB5 in humans and
686 their corresponding mapped cell types in mice and macaques, gene symbols of the raw count
687 matrices of mouse and macaque data were converted into human orthologs using the MGI¹⁰²
688 and HGNC¹⁰³ databases. Utilizing human gene symbols and orthologs, cell type similarities
689 were computed in a manner similar to the comparison of cell types between snRNA-seq and
690 scRNA-seq datasets utilizing the MetaNeighbor R package⁹⁵.
691

692 **Marker identification by binary classification analysis**

693 To identify novel markers for BC, AC, and RGC types, a binary classification approach
694 was applied to detect 2- or 3-marker combinations for each type¹³. To mitigate classification
695 bias resulting from unbalanced cell type abundances, up to 2000 cells were randomly sampled
696 for BC types, and up to 500 cells were sampled for AC and RGC clusters. First, the raw counts
697 were normalized, and the top 50 ranked genes were calculated for each cell type using the
698 Scanpy package⁹¹. Support vector classifiers were then trained by considering combinations
699 of the top-ranked genes for each cell type. The “SVC()” function with “kernel=rbf” was
700 employed from the scikit-learn Python package¹⁰⁴. Combinations of markers were ranked
701 based on several classification metrics, including precision, recall, F1 score, and AUROC.
702

703 **Annotation of snATAC-seq cells and co-embedding of snATAC-seq and snRNA-seq 704 cells**

705 To annotate cell types for snATAC-seq, the low-quality cells and doublets were first
706 filtered out, and the retained cells were clustered with ArchR¹⁰⁵ (minTSS=4, minFrags=1000,
707 filterRatio=1). By integrating with snRNA-seq data, six major neuron cell classes and a mixed
708 non-neuron cell class were identified through ArchR. Then peaks were called by MACS2¹⁰⁶
709 through ArchR and cell by peak fragment count matrices were generated for each of the major
710 cell classes and across major cell classes via Seurat⁸⁹ and Signac¹⁰⁷. The co-embedding of
711 snRNA-seq and snATAC-seq was performed with the GLUE algorithm³⁹. Specifically, to
712 integrate major cell class annotation, all snATAC-seq cells were co-embedded with the down-
713 sampled snRNA-seq cells by scGlue under the supervised mode, since major cell classes
714 from both snATAC-seq and snRNA-seq were already annotated. However, to identify cell
715 types per major class, the snATAC-seq cells were co-embedded with the snRNA-seq cells for
716 a major class by scGlue under the unsupervised mode. A logistic regression model and an
717 SVM model were then trained using the GLUE embedding and annotation of snRNA-seq cells
718 to predict the cell types of snATAC-seq cells using the scikit-learn python package. The ROC-
719 AUC of the logistic regression model was consistently higher than that of SVM model, so the

720 logistic regression model was used to annotate snATAC-seq cells. The peaks were called by
721 MACS2 through ArchR for snATAC-seq cell classes and types. Differentially accessible
722 regions (DARs) and linked CREs were identified across cell classes and types using ArchR.
723 The linked CREs were the union set of peak-gene pairs identified through the correlation of
724 accessibility between snATAC-seq peaks (-/+ 250kb surrounding TSS) and promoters (co-
725 accessibility), as well as the correlation between gene expression and the accessibility of
726 snATAC-seq peaks (-/+ 250kb surrounding TSS).

727

728 **Identification of regulon of retinal cell types**

729 Regulons were identified for each of major cell classes, subclasses, and cell types
730 respectively utilizing SCENIC+³¹. Since SCENIC+ is memory-demanding, up to 1,000, 2,000,
731 or 4,000 cells per cell type (depending on specific cell class/subclass/type) were down-
732 sampled for snATAC-seq cells and snRNA-seq cells respectively. The down-sampled cell by
733 gene matrices and cell by peak matrices were then submitted to SCENIC+. Transcription
734 factors (TF), target regions of TFs, and target genes of TFs were also identified across cell
735 types. The transcription factors that showed significant correlation between gene expression
736 and chromatin accessibility of the target regions across cell types were further selected as
737 candidate TFs. From these TFs, eRegulon Specificity Score (RSS) was also computed for the
738 TFs that were identified as activators in the corresponding cell type. Furthermore, the TFs that
739 displayed a significant correlation between the accessibility of target regions and the
740 expression level of target genes were identified. Subsequently, TF modules displaying a
741 significant correlation in the region-based AUC between TFs were identified.

742

743 **Massively parallel reporter assays**

744 We developed a MPRA library, which contains the sequences of 1,820 CRE
745 candidates linked to inherited retinal disease genes identified in the rod cells, along with 20
746 control cis-regulatory elements (CREs) with a variety of activity that have been previously
747 validated⁸⁰, and negative controls (i.e., 300 scrambled sequences, and a basal promoter
748 without CRE). Each CRE or control sequence was labeled with three unique barcodes, and
749 25 barcodes were assigned to the basal promoter. Oligonucleotides (oligos) were synthesized
750 as follows: 5' priming sequence /EcoRI site/Library sequence (224-bp)/Spel site/C/SphI
751 site/Barcode sequence (9-bp)/NotI site/3' priming sequence. These oligomers were ordered
752 from TWIST BIOSCIENCE (South San Francisco, CA) and cloned upstream of a
753 photoreceptor-specific Crx promoter, which drives the expression of a DsRed reporter gene.
754 The resulting plasmid library was then electroporated into three retinal explants of C57BL/6J

755 mice at postnatal day 0 (P0) in four replicates. On Day 8, DNA and RNA were extracted from
756 the cultured explants and next-generation sequencing was conducted. The activity of each
757 CRE was calculated based on the ratio of RNA/DNA read counts and was normalized to the
758 activity of the basal Crx promoter. The bioinformatics analysis of the MPRA result followed the
759 previously published pipeline⁸⁰.

760

761 **Differential gene expression analysis during aging and between genders**

762 We conducted two types of differential gene expression analysis during aging. First,
763 for each cell class, raw read counts were aggregated per gene per sample. Only the samples
764 containing at least 100 cells in the corresponding cell class were considered. Additionally, the
765 samples that had < 0.75 correlation in read counts with $> 65\%$ of samples were considered
766 as outliers and were not included in subsequent analysis. Genes with low expression in the
767 corresponding cell classes were filtered out, resulting in about 18,003 genes retained per cell
768 class for further analysis. Based on the filtered genes and samples, the genes significantly
769 correlated with aging and different between sexes were identified using a mixed linear effect
770 model via edgeR¹⁰⁸ and variancePartition¹⁰⁹ R packages. The formula we applied were: \sim
771 age + sex + race + tissue + seq+ (1|batch) for age and sex effect, and \sim age + sex + race +
772 tissue + seq+ (age:sex) + (1|batch) for the interaction between age and sex. Log2 fold change
773 and *p*-values were extracted for all genes for the covariate of interest, i.e., age, sex, and
774 interaction between age and sex. In addition, a sliding window analysis was conducted over
775 aging, and DEGs between two adjacent time windows were identified per cell class utilizing
776 the DEswan R package¹¹⁰. The read counts of the filtered genes were normalized based on
777 the library size of each sample per cell class via the edgeR R package. The sliding window
778 analysis was conducted over aging, considering batch and sex as covariates at the age: 20,
779 30, 40, 50, 60, 70, 80, and 90, with the bucket size = 20 years. In all time windows (10-year
780 interval) except three windows in RGC, there are more than three samples per cell class,
781 ensuring statistical robustness. Enriched pathways and GO terms were identified through
782 gene set enrichment analysis of the differentially expressed genes utilizing the clusterProfiler
783 R package⁹⁸. The significance cutoff for enriched gene sets was set at FDR < 0.1 .

784

785 **Cell type enrichment underlying GWAS locus**

786 Cell class enrichment underlying GWAS loci was identified based on both chromatin
787 accessibility and gene expression. For chromatin accessibility, the heritability of GWAS traits
788 were partitioned into cell class specific snATAC-seq peaks using stratified LD score regression
789 via LDSC⁶¹. Initially, GWAS SNPs that overlapped with HapMap3 SNPs were annotated

790 based on whether they were in OCRs in each cell class. Subsequently, LD-scores of these
791 SNPs within 1 cM windows were calculated based on the 1000 Genome data. The LD-scores
792 of these SNPs were integrated with those from the baseline model, which included non-cell
793 type specific annotation (downloaded from <https://alkesgroup.broadinstitute.org/LDSCORE/>).
794 Finally, the heritability in the annotated genomic regions was estimated and compared with
795 the baseline model to determine if regions in each cell class were enriched with the heritability
796 of the corresponding GWAS trait. For gene expression, the linear positive correlation between
797 cell class specificity of gene expression and gene-level genetic association with GWAS
798 studies were assessed by using the MAGMA.Celltype R package ⁶². GWAS summary
799 statistics were formatted with the “MungeSumstats” R package ¹¹¹ based on SNPs in -
800 35kb/+10kb of each gene and 1000 genome “eur” population. snRNA-seq expression data
801 was formatted with the “EWCE” R package ¹¹². Linear enrichment was detected using the
802 MAGMA.Celltype R package. To correct for multiple testing, the Benjamini-Hochberg method
803 was applied to the enrichment *p*-value based on chromatin accessibility and gene expression
804 respectively, considering the number of cell types and GWAS studies tested.

805

806 **Fine-mapping of GWAS and eQTL variants**

807 GWAS loci were fine-mapped based on the summary statistics of GWAS studies. For
808 each GWAS study, the SNPs with $p < 5 \times 10^{-8}$ and present in 1000 genome (phase 3)
809 European population were considered and were categorized into the LD blocks identified by
810 a previous study. Within each LD block, the posterior inclusion probability (PIP) of each SNP
811 and credible set of SNPs were calculated using the susieR package (L=10) ¹¹³. Similarly, eQTL
812 variants were fine-mapped based on the summary statistics of bulk retinal eQTLs. The
813 colocalization analysis of GWAS signal and bulk eQTL signal was conducted using the coloc
814 R package ¹¹⁴. The motif disrupt effect of SNPs was predicted by the motifbreakR R package
815 ¹¹⁵.

816

817 **Query to reference mapping using scArches**

818 The HRCA cell type labeling enables automated cell type annotation using scArches
819 ⁸¹. We trained query-to-reference models using scArches, using default parameters as
820 recommended in their core tutorials. Models were trained during 20 epochs for scVI, scANVI,
821 and label transfer on sc and sn cells from the healthy reference and using batch information
822 during the integration benchmark. Additional cell type sub-annotations were used, based on
823 clustering and marker-based selection per major classes. Only healthy donors were
824 considered to generate reference models.

825 To test the cell mapping and uncertainty estimations in new samples, we used age-
826 related macular degeneration samples (AMD) related to 17 donors. As validation of the label
827 transfer accuracy, we pre-annotated one of the disease samples using scPred, obtaining 98%
828 agreement in labels. Label uncertainties per major class mapped on AMD donors were
829 analyzed as a single-variable distribution, and we defined a percentile threshold of 97.5% to
830 label cells as high- or low-uncertainty based on this value. Selection of visualization of marker
831 genes across categories was done on each cell type, between both uncertainty categories,
832 using Scanpy ⁹¹. Overlap between selected marker genes AMD-related genes was inspected
833 using the ontology term Macular Degeneration (DOID:4448) from the DISEASES database ¹¹⁶.
834

835 **Data availability**

836 The landing page of the HRCA data resources is accessible at
837 <https://rchenlab.github.io/resources/human-atlas.html>. Raw sequencing data files, processed
838 Cell Ranger data files, and sample metadata information files of the HRCA have been
839 deposited in the HCA DCP. Additionally, raw and normalized count matrices, cell type
840 annotations, and multi-omics embeddings are also publicly available through the CELLxGENE
841 collection (<https://cellxgene.cziscience.com/collections/4c6eaf5c-6d57-4c76-b1e9-60df8c655f1e>). The HRCA is also accessible at the UCSC Cell Browser (<https://cellstest.gi.ucsc.edu/?ds=retina-atlas+rna-seq+chen>) and the Single Cell Portal.
842

843

844 **Code availability**

845 All code used for the HRCA project can be found in the HRCA reproducibility GitHub
846 repository (https://github.com/RCHENLAB/HRCA_reproducibility). The pipeline to process the
847 unpublished and collected public datasets is accessible at <https://github.com/ljinbio/cellqc>.
848 Scripts related to the benchmark study, integration pipeline, and label transfer using scArches
849 are available at <https://github.com/theislab/HRCA-reproducibility>.
850

851

852 **Acknowledgements**

853 This project was funded by the Chan Zuckerberg Initiative (CZI) 2019-002425 and
854 2021-239847 to R.C., and CZI 2021-237885 to T.S. Additionally, next-generation sequencing
855 (NGS) was performed on instrument supported by the National Institutes of Health (NIH)
856 shared instrument grant S10OD023469 to R.C. This work was also funded by NIH EY028633
857 and U01 MH105960 and CZI award CZF-2019-002459 to J.R.S., and NIH/NEI EY012543 (to
858 SC) and EY002687 (to WU-DOVS). This publication is part of the Human Cell Atlas

859 (http://www.humancellatlas.org/publications/). We would also like to acknowledge the
860 feedback and discussions from the members of the HCA Eye Biological Network.

861

862 **Author contributions**

863 J.L., J.W., and R.C. conceptualized and designed the study. R.C. supervised the work.
864 M.M.D. and J.T.S. collected samples. X.C. and Y.L. generated snRNA-seq and snATAC-seq
865 data in this study. I.L.I. performed the benchmark study for data integration of RNA-seq
866 datasets in this study and label transfer analyses. J.L. and J.W. compiled dataset collection
867 for public snRNA-seq/scRNA-seq and snATAC-seq datasets. J.L. performed data integration
868 for RNA-seq datasets. J.W. performed data integration for ATAC-seq datasets. J.L. performed
869 atlas construction, annotation, and data dissemination of the atlas. J.W. conducted multi-
870 omics analysis, gene expression across covariates, and genetic variants analysis. I.L.I.,
871 M.D.L., and F.J.T. provided input to various analysis methods. N.M.T. and K.S. provided input
872 for various annotations. A.M., W.Y. and J.R.S. collected, analyzed and provided processed
873 data from an unpublished dataset. Y.Z. and S.C. advised and performed massively parallel
874 reporter assays in mouse retina. J.L. and J.W. wrote the first draft of the manuscript. All
875 authors edited the manuscript and contributed to critical revisions of the manuscript.

876

877 **Competing interests**

878 F.J.T. consults for Immunai Inc., CytoReason Ltd, Cellarity Inc and Omniscope Ltd, and
879 owns interests in Dermagnostix GmbH and Cellarity Inc. Other authors declare no competing
880 interests.

881

882 **References:**

883 1 Regev, A. *et al.* The Human Cell Atlas. *Elife* **6** (2017).
<https://doi.org/10.7554/eLife.27041>

884 2 Rozenblatt-Rosen, O., Stubbington, M. J. T., Regev, A. & Teichmann, S. A. The
885 Human Cell Atlas: from vision to reality. *Nature* **550**, 451-453 (2017).
<https://doi.org/10.1038/550451a>

886 3 Sikkema, L. *et al.* An integrated cell atlas of the lung in health and disease. *Nat
Med* **29**, 1563-1577 (2023). <https://doi.org/10.1038/s41591-023-02327-2>

887 4 Kumar, T. *et al.* A spatially resolved single-cell genomic atlas of the adult human
888 breast. *Nature* **620**, 181-191 (2023). [https://doi.org/10.1038/s41586-023-06252-9](https://doi.org/10.1038/s41586-023-
06252-9)

889 5 van Zyl, T. *et al.* Cell atlas of the human ocular anterior segment: Tissue-
890 specific and shared cell types. *Proc Natl Acad Sci U S A* **119**, e2200914119
891 (2022). <https://doi.org/10.1073/pnas.2200914119>

892 6 Monavarfeshani, A. *et al.* Transcriptomic analysis of the ocular posterior
893 segment completes a cell atlas of the human eye. *Proc Natl Acad Sci U S A*
894 **120**, e2306153120 (2023). <https://doi.org/10.1073/pnas.2306153120>

895 7 Liang, Q. *et al.* A multi-omics atlas of the human retina at single-cell resolution.
896 *Cell Genomics*, 100298 (2023).
<https://doi.org/https://doi.org/10.1016/j.xgen.2023.100298>

897 8 Hahn, J. *et al.* Evolution of neuronal cell classes and types in the vertebrate
898 retina. *bioRxiv* (2023). <https://doi.org/10.1101/2023.04.07.536039>

899 9 Peng, Y. R. *et al.* Molecular Classification and Comparative Taxonomics of
900 Foveal and Peripheral Cells in Primate Retina. *Cell* **176**, 1222-1237 e1222
901 (2019). <https://doi.org/10.1016/j.cell.2019.01.004>

902 10 Yamagata, M., Yan, W. & Sanes, J. R. A cell atlas of the chick retina based on
903 single-cell transcriptomics. *Elife* **10** (2021). <https://doi.org/10.7554/eLife.63907>

904 11 Macosko, E. Z. *et al.* Highly Parallel Genome-wide Expression Profiling of
905 Individual Cells Using Nanoliter Droplets. *Cell* **161**, 1202-1214 (2015).
<https://doi.org/10.1016/j.cell.2015.05.002>

906 12 Shekhar, K. *et al.* Comprehensive Classification of Retinal Bipolar Neurons by
907 Single-Cell Transcriptomics. *Cell* **166**, 1308-1323 e1330 (2016).
<https://doi.org/10.1016/j.cell.2016.07.054>

908 13 Tran, N. M. *et al.* Single-Cell Profiles of Retinal Ganglion Cells Differing in
909 Resilience to Injury Reveal Neuroprotective Genes. *Neuron* **104**, 1039-1055
910 e1012 (2019). <https://doi.org/10.1016/j.neuron.2019.11.006>

911 14 Yan, W. *et al.* Mouse Retinal Cell Atlas: Molecular Identification of over Sixty
912 Amacrine Cell Types. *J Neurosci* **40**, 5177-5195 (2020).
<https://doi.org/10.1523/JNEUROSCI.0471-20.2020>

913 15 Yan, W. *et al.* Cell Atlas of The Human Fovea and Peripheral Retina. *Sci Rep*
914 **10**, 9802 (2020). <https://doi.org/10.1038/s41598-020-66092-9>

915 16 Buenrostro, J. D. *et al.* Single-cell chromatin accessibility reveals principles of
916 regulatory variation. *Nature* **523**, 486-490 (2015).
<https://doi.org/10.1038/nature14590>

917 17 Luecken, M. D. *et al.* Benchmarking atlas-level data integration in single-cell
918 genomics. *Nat Methods* **19**, 41-50 (2022). [https://doi.org/10.1038/s41592-021-01336-8](https://doi.org/10.1038/s41592-021-
01336-8)

929 18 Luecken, M. D. *et al.* in *Thirty-fifth conference on neural information processing*
930 *systems datasets and benchmarks track (Round 2)*.

931 19 Cowan, C. S. *et al.* Cell Types of the Human Retina and Its Organoids at Single-
932 Cell Resolution. *Cell* **182**, 1623-1640 e1634 (2020).
<https://doi.org/10.1016/j.cell.2020.08.013>

934 20 Orozco, L. D. *et al.* Integration of eQTL and a Single-Cell Atlas in the Human
935 Eye Identifies Causal Genes for Age-Related Macular Degeneration. *Cell Rep*
936 **30**, 1246-1259 e1246 (2020). <https://doi.org/10.1016/j.celrep.2019.12.082>

937 21 Lukowski, S. W. *et al.* A single-cell transcriptome atlas of the adult human retina.
938 *EMBO J* **38**, e100811 (2019). <https://doi.org/10.1525/embj.2018100811>

939 22 Menon, M. *et al.* Single-cell transcriptomic atlas of the human retina identifies
940 cell types associated with age-related macular degeneration. *Nat Commun* **10**,
941 4902 (2019). <https://doi.org/10.1038/s41467-019-12780-8>

942 23 Voigt, A. P. *et al.* Molecular characterization of foveal versus peripheral human
943 retina by single-cell RNA sequencing. *Exp Eye Res* **184**, 234-242 (2019).
<https://doi.org/10.1016/j.exer.2019.05.001>

945 24 Lopez, R., Regier, J., Cole, M. B., Jordan, M. I. & Yosef, N. Deep generative
946 modeling for single-cell transcriptomics. *Nat Methods* **15**, 1053-1058 (2018).
<https://doi.org/10.1038/s41592-018-0229-2>

948 25 Santiago, C. P. *et al.* Comparative Analysis of Single-cell and Single-nucleus
949 RNA-sequencing in a Rabbit Model of Retinal Detachment-related Proliferative
950 Vitreoretinopathy. *Ophthalmol Sci* **3**, 100335 (2023).
<https://doi.org/10.1016/j.xops.2023.100335>

952 26 Rosen, Y. *et al.* Towards Universal Cell Embeddings: Integrating Single-cell
953 RNA-seq Datasets across Species with SATURN. *bioRxiv* (2023).
<https://doi.org/10.1101/2023.02.03.526939>

955 27 Bakken, T. E. *et al.* Single-cell and single-nucleus RNA-seq uncovers shared
956 and distinct axes of variation in dorsal LGN neurons in mice, non-human
957 primates, and humans. *eLife* **10** (2021). <https://doi.org/10.7554/eLife.64875>

958 28 Kolb, H., Fernandez, E. & Nelson, R. Webvision: the organization of the retina
959 and visual system [Internet]. (1995).

960 29 Hughes, A. E. O., Myers, C. A. & Corbo, J. C. A massively parallel reporter
961 assay reveals context-dependent activity of homeodomain binding sites in vivo.
962 *Genome Res* **28**, 1520-1531 (2018). <https://doi.org/10.1101/gr.231886.117>

963 30 Shepherdson, J. L. *et al.* Pathogenic variants in CRX have distinct cis -
964 regulatory effects on enhancers and silencers in photoreceptors. *bioRxiv* (2023).
<https://doi.org/10.1101/2023.05.27.542576>

966 31 Bravo Gonzalez-Blas, C. *et al.* SCENIC+: single-cell multiomic inference of
967 enhancers and gene regulatory networks. *Nat Methods* **20**, 1355-1367 (2023).
<https://doi.org/10.1038/s41592-023-01938-4>

969 32 de Melo, J. *et al.* Lhx2 Is an Essential Factor for Retinal Gliogenesis and Notch
970 Signaling. *J Neurosci* **36**, 2391-2405 (2016).
<https://doi.org/10.1523/JNEUROSCI.3145-15.2016>

972 33 Sapkota, D. *et al.* Onecut1 and Onecut2 redundantly regulate early retinal cell
973 fates during development. *Proc Natl Acad Sci U S A* **111**, E4086-4095 (2014).
<https://doi.org/10.1073/pnas.1405354111>

975 34 Clark, B. S. *et al.* Single-Cell RNA-Seq Analysis of Retinal Development
976 Identifies NFI Factors as Regulating Mitotic Exit and Late-Born Cell

977 Specification. *Neuron* **102**, 1111-1126 e1115 (2019).
978 <https://doi.org/10.1016/j.neuron.2019.04.010>

979 35 Yamamoto, H., Kon, T., Omori, Y. & Furukawa, T. Functional and Evolutionary
980 Diversification of Otx2 and Crx in Vertebrate Retinal Photoreceptor and Bipolar
981 Cell Development. *Cell Rep* **30**, 658-671 e655 (2020).
982 <https://doi.org/10.1016/j.celrep.2019.12.072>

983 36 Remez, L. A. *et al.* Pax6 is essential for the generation of late-born retinal
984 neurons and for inhibition of photoreceptor-fate during late stages of
985 retinogenesis. *Dev Biol* **432**, 140-150 (2017).
986 <https://doi.org/10.1016/j.ydbio.2017.09.030>

987 37 Cheng, H. *et al.* Photoreceptor-specific nuclear receptor NR2E3 functions as a
988 transcriptional activator in rod photoreceptors. *Hum Mol Genet* **13**, 1563-1575
989 (2004). <https://doi.org/10.1093/hmg/ddh173>

990 38 Kaewkhaw, R. *et al.* Transcriptome Dynamics of Developing Photoreceptors in
991 Three-Dimensional Retina Cultures Recapitulates Temporal Sequence of
992 Human Cone and Rod Differentiation Revealing Cell Surface Markers and
993 Gene Networks. *Stem Cells* **33**, 3504-3518 (2015).
994 <https://doi.org/10.1002/stem.2122>

995 39 Cao, Z. J. & Gao, G. Multi-omics single-cell data integration and regulatory
996 inference with graph-linked embedding. *Nat Biotechnol* **40**, 1458-1466 (2022).
997 <https://doi.org/10.1038/s41587-022-01284-4>

998 40 Campello, L. *et al.* Aging of the Retina: Molecular and Metabolic Turbulences
999 and Potential Interventions. *Annu Rev Vis Sci* **7**, 633-664 (2021).
1000 <https://doi.org/10.1146/annurev-vision-100419-114940>

1001 41 Aniniye, I. O. *et al.* The roles of sex and gender in women's eye health disparities
1002 in the United States. *Biol Sex Differ* **12**, 57 (2021).
1003 <https://doi.org/10.1186/s13293-021-00401-3>

1004 42 Park, D. H., Connor, K. M. & Lambris, J. D. The Challenges and Promise of
1005 Complement Therapeutics for Ocular Diseases. *Front Immunol* **10**, 1007 (2019).
1006 <https://doi.org/10.3389/fimmu.2019.01007>

1007 43 Khandhadia, S., Cipriani, V., Yates, J. R. & Lotery, A. J. Age-related macular
1008 degeneration and the complement system. *Immunobiology* **217**, 127-146
1009 (2012). <https://doi.org/10.1016/j.imbio.2011.07.019>

1010 44 Armento, A., Ueffing, M. & Clark, S. J. The complement system in age-related
1011 macular degeneration. *Cell Mol Life Sci* **78**, 4487-4505 (2021).
1012 <https://doi.org/10.1007/s00018-021-03796-9>

1013 45 Geerlings, M. J., de Jong, E. K. & den Hollander, A. I. The complement system
1014 in age-related macular degeneration: A review of rare genetic variants and
1015 implications for personalized treatment. *Mol Immunol* **84**, 65-76 (2017).
1016 <https://doi.org/10.1016/j.molimm.2016.11.016>

1017 46 Ma, H., Yang, F. & Ding, X. Q. Inhibition of thyroid hormone signaling protects
1018 retinal pigment epithelium and photoreceptors from cell death in a mouse model
1019 of age-related macular degeneration. *Cell Death Dis* **11**, 24 (2020).
1020 <https://doi.org/10.1038/s41419-019-2216-7>

1021 47 Xu, H. & Chen, M. Targeting the complement system for the management of
1022 retinal inflammatory and degenerative diseases. *Eur J Pharmacol* **787**, 94-104
1023 (2016). <https://doi.org/10.1016/j.ejphar.2016.03.001>

1024 48 Nuzzi, R., Scalabrin, S., Becco, A. & Panzica, G. Gonadal Hormones and
1025 Retinal Disorders: A Review. *Front Endocrinol (Lausanne)* **9**, 66 (2018).
1026 <https://doi.org/10.3389/fendo.2018.00066>

1027 49 Liu, K. *et al.* Genetic variation reveals the influence of steroid hormones on the
1028 risk of retinal neurodegenerative diseases. *Front Endocrinol (Lausanne)* **13**,
1029 1088557 (2022). <https://doi.org/10.3389/fendo.2022.1088557>

1030 50 Lu, T. C. *et al.* Aging Fly Cell Atlas identifies exhaustive aging features at
1031 cellular resolution. *Science* **380**, eadg0934 (2023).
<https://doi.org/10.1126/science.adg0934>

1033 51 Whitacre, C. C., Reingold, S. C. & O'Looney, P. A. A gender gap in
1034 autoimmunity. *Science* **283**, 1277-1278 (1999).
<https://doi.org/10.1126/science.283.5406.1277>

1036 52 Beeson, P. B. Age and sex associations of 40 autoimmune diseases. *Am J Med*
1037 **96**, 457-462 (1994). [https://doi.org/10.1016/0002-9343\(94\)90173-2](https://doi.org/10.1016/0002-9343(94)90173-2)

1038 53 Oertelt-Prigione, S. The influence of sex and gender on the immune response.
1039 *Autoimmun Rev* **11**, A479-485 (2012).
<https://doi.org/10.1016/j.autrev.2011.11.022>

1041 54 Ansar Ahmed, S., Penhale, W. J. & Talal, N. Sex hormones, immune responses,
1042 and autoimmune diseases. Mechanisms of sex hormone action. *Am J Pathol*
1043 **121**, 531-551 (1985).

1044 55 Huan, T. *et al.* Identifying Novel Genes and Variants in Immune and
1045 Coagulation Pathways Associated with Macular Degeneration. *Ophthalmol Sci*
1046 **3**, 100206 (2023). <https://doi.org/10.1016/j.xops.2022.100206>

1047 56 Rudnicka, A. R. *et al.* Age and gender variations in age-related macular
1048 degeneration prevalence in populations of European ancestry: a meta-analysis.
1049 *Ophthalmology* **119**, 571-580 (2012).
<https://doi.org/10.1016/j.ophtha.2011.09.027>

1051 57 Li, M. *et al.* Autophagy in glaucoma pathogenesis: Therapeutic potential and
1052 future perspectives. *Front Cell Dev Biol* **10**, 1068213 (2022).
<https://doi.org/10.3389/fcell.2022.1068213>

1054 58 Dixon, A. *et al.* Autophagy deficiency protects against ocular hypertension and
1055 neurodegeneration in experimental and spontaneous glaucoma mouse models.
1056 *Cell Death Dis* **14**, 554 (2023). <https://doi.org/10.1038/s41419-023-06086-3>

1057 59 Kapetanakis, V. V. *et al.* Global variations and time trends in the prevalence of
1058 primary open angle glaucoma (POAG): a systematic review and meta-analysis.
1059 *Br J Ophthalmol* **100**, 86-93 (2016). <https://doi.org/10.1136/bjophthalmol-2015-307223>

1061 60 Zhang, N., Wang, J., Li, Y. & Jiang, B. Prevalence of primary open angle
1062 glaucoma in the last 20 years: a meta-analysis and systematic review. *Sci Rep*
1063 **11**, 13762 (2021). <https://doi.org/10.1038/s41598-021-92971-w>

1064 61 Finucane, H. K. *et al.* Partitioning heritability by functional annotation using
1065 genome-wide association summary statistics. *Nat Genet* **47**, 1228-1235 (2015).
1066 <https://doi.org/10.1038/ng.3404>

1067 62 de Leeuw, C. A., Mooij, J. M., Heskes, T. & Posthuma, D. MAGMA: generalized
1068 gene-set analysis of GWAS data. *PLoS Comput Biol* **11**, e1004219 (2015).
1069 <https://doi.org/10.1371/journal.pcbi.1004219>

1070 63 Fritsche, L. G. *et al.* A large genome-wide association study of age-related
1071 macular degeneration highlights contributions of rare and common variants.
1072 *Nat Genet* **48**, 134-143 (2016). <https://doi.org/10.1038/ng.3448>

1073 64 Currant, H. *et al.* Sub-cellular level resolution of common genetic variation in
1074 the photoreceptor layer identifies continuum between rare disease and
1075 common variation. *PLoS Genet* **19**, e1010587 (2023).
1076 <https://doi.org/10.1371/journal.pgen.1010587>

1077 65 Gharahkhani, P. *et al.* Genome-wide meta-analysis identifies 127 open-angle
1078 glaucoma loci with consistent effect across ancestries. *Nat Commun* **12**, 1258
1079 (2021). <https://doi.org/10.1038/s41467-020-20851-4>

1080 66 Khawaja, A. P. *et al.* Genome-wide analyses identify 68 new loci associated
1081 with intraocular pressure and improve risk prediction for primary open-angle
1082 glaucoma. *Nat Genet* **50**, 778-782 (2018). <https://doi.org/10.1038/s41588-018-0126-8>

1084 67 Springelkamp, H. *et al.* New insights into the genetics of primary open-angle
1085 glaucoma based on meta-analyses of intraocular pressure and optic disc
1086 characteristics. *Hum Mol Genet* **26**, 438-453 (2017).
1087 <https://doi.org/10.1093/hmg/ddw399>

1088 68 Hysi, P. G. *et al.* Meta-analysis of 542,934 subjects of European ancestry
1089 identifies new genes and mechanisms predisposing to refractive error and
1090 myopia. *Nat Genet* **52**, 401-407 (2020). <https://doi.org/10.1038/s41588-020-0599-0>

1092 69 Kemp, J. P. *et al.* Identification of 153 new loci associated with heel bone
1093 mineral density and functional involvement of GPC6 in osteoporosis. *Nat Genet*
1094 **49**, 1468-1475 (2017). <https://doi.org/10.1038/ng.3949>

1095 70 Jiang, L., Zheng, Z., Fang, H. & Yang, J. A generalized linear mixed model
1096 association tool for biobank-scale data. *Nat Genet* **53**, 1616-1621 (2021).
1097 <https://doi.org/10.1038/s41588-021-00954-4>

1098 71 Collantes, E. R. A. *et al.* EFEMP1 rare variants cause familial juvenile-onset
1099 open-angle glaucoma. *Hum Mutat* **43**, 240-252 (2022).
1100 <https://doi.org/10.1002/humu.24320>

1101 72 Liu, Y. & Allingham, R. R. Major review: Molecular genetics of primary open-
1102 angle glaucoma. *Exp Eye Res* **160**, 62-84 (2017).
1103 <https://doi.org/10.1016/j.exer.2017.05.002>

1104 73 Guo, F. *et al.* ABCF1 extrinsically regulates retinal pigment epithelial cell
1105 phagocytosis. *Mol Biol Cell* **26**, 2311-2320 (2015).
1106 <https://doi.org/10.1091/mbc.E14-09-1343>

1107 74 Youngblood, H., Robinson, R., Sharma, A. & Sharma, S. Proteomic Biomarkers
1108 of Retinal Inflammation in Diabetic Retinopathy. *Int J Mol Sci* **20** (2019).
1109 <https://doi.org/10.3390/ijms20194755>

1110 75 Lu, Y. *et al.* Single-Cell Analysis of Human Retina Identifies Evolutionarily
1111 Conserved and Species-Specific Mechanisms Controlling Development. *Dev
1112 Cell* **53**, 473-491 e479 (2020). <https://doi.org/10.1016/j.devcel.2020.04.009>

1113 76 Muranishi, Y. *et al.* An essential role for RAX homeoprotein and NOTCH-HES
1114 signaling in Otx2 expression in embryonic retinal photoreceptor cell fate
1115 determination. *J Neurosci* **31**, 16792-16807 (2011).
1116 <https://doi.org/10.1523/JNEUROSCI.3109-11.2011>

1117 77 Megill, C. *et al.* cellxgene: a performant, scalable exploration platform for high
1118 dimensional sparse matrices. *bioRxiv*, 2021.2004.2005.438318 (2021).
1119 <https://doi.org/10.1101/2021.04.05.438318>

1120 78 Speir, M. L. *et al.* UCSC Cell Browser: visualize your single-cell data.
1121 *Bioinformatics* **37**, 4578-4580 (2021).
1122 <https://doi.org/10.1093/bioinformatics/btab503>

1123 79 Tarhan, L. *et al.* Single Cell Portal: an interactive home for single-cell genomics
1124 data. *bioRxiv* (2023). <https://doi.org/10.1101/2023.07.13.548886>

1125 80 Friedman, R. Z. *et al.* Information content differentiates enhancers from
1126 silencers in mouse photoreceptors. *Elife* **10** (2021).
1127 <https://doi.org/10.7554/elife.67403>

1128 81 Lotfollahi, M. *et al.* Mapping single-cell data to reference atlases by transfer
1129 learning. *Nat Biotechnol* **40**, 121-130 (2022). <https://doi.org/10.1038/s41587-021-01001-7>

1131 82 Owen, L. A. *et al.* The Utah Protocol for Postmortem Eye Phenotyping and
1132 Molecular Biochemical Analysis. *Invest Ophthalmol Vis Sci* **60**, 1204-1212
1133 (2019). <https://doi.org/10.1167/iovs.18-24254>

1134 83 Zheng, G. X. *et al.* Massively parallel digital transcriptional profiling of single
1135 cells. *Nat Commun* **8**, 14049 (2017). <https://doi.org/10.1038/ncomms14049>

1136 84 Lun, A. T. L. *et al.* EmptyDrops: distinguishing cells from empty droplets in
1137 droplet-based single-cell RNA sequencing data. *Genome Biol* **20**, 63 (2019).
1138 <https://doi.org/10.1186/s13059-019-1662-y>

1139 85 Heiser, C. N., Wang, V. M., Chen, B., Hughey, J. J. & Lau, K. S. Automated
1140 quality control and cell identification of droplet-based single-cell data using
1141 dropkick. *Genome Res* **31**, 1742-1752 (2021).
1142 <https://doi.org/10.1101/gr.271908.120>

1143 86 Young, M. D. & Behjati, S. SoupX removes ambient RNA contamination from
1144 droplet-based single-cell RNA sequencing data. *Gigascience* **9** (2020).
1145 <https://doi.org/10.1093/gigascience/giaa151>

1146 87 McGinnis, C. S., Murrow, L. M. & Gartner, Z. J. DoubletFinder: Doublet
1147 Detection in Single-Cell RNA Sequencing Data Using Artificial Nearest
1148 Neighbors. *Cell Syst* **8**, 329-337 e324 (2019).
1149 <https://doi.org/10.1016/j.cels.2019.03.003>

1150 88 Alquicira-Hernandez, J., Sathe, A., Ji, H. P., Nguyen, Q. & Powell, J. E. scPred:
1151 accurate supervised method for cell-type classification from single-cell RNA-
1152 seq data. *Genome Biol* **20**, 264 (2019). <https://doi.org/10.1186/s13059-019-1862-5>

1154 89 Stuart, T. *et al.* Comprehensive Integration of Single-Cell Data. *Cell* **177**, 1888-
1155 1902 e1821 (2019). <https://doi.org/10.1016/j.cell.2019.05.031>

1156 90 Hao, Y. *et al.* Integrated analysis of multimodal single-cell data. *Cell* **184**, 3573-
1157 3587 e3529 (2021). <https://doi.org/10.1016/j.cell.2021.04.048>

1158 91 Wolf, F. A., Angerer, P. & Theis, F. J. SCANPY: large-scale single-cell gene
1159 expression data analysis. *Genome Biol* **19**, 15 (2018).
1160 <https://doi.org/10.1186/s13059-017-1382-0>

1161 92 Traag, V. A., Waltman, L. & van Eck, N. J. From Louvain to Leiden:
1162 guaranteeing well-connected communities. *Sci Rep* **9**, 5233 (2019).
1163 <https://doi.org/10.1038/s41598-019-41695-z>

1164 93 McInnes, L., Healy, J. & Melville, J. Umap: Uniform manifold approximation and
1165 projection for dimension reduction. *arXiv preprint arXiv:1802.03426* (2018).

1166 94 Miao, Z. *et al.* Putative cell type discovery from single-cell gene expression data.
1167 *Nat Methods* **17**, 621-628 (2020). <https://doi.org/10.1038/s41592-020-0825-9>

1168 95 Crow, M., Paul, A., Ballouz, S., Huang, Z. J. & Gillis, J. Characterizing the
1169 replicability of cell types defined by single cell RNA-sequencing data using
1170 MetaNeighbor. *Nat Commun* **9**, 884 (2018). <https://doi.org/10.1038/s41467-018-03282-0>

1172 96 Love, M. I., Huber, W. & Anders, S. Moderated estimation of fold change and
1173 dispersion for RNA-seq data with DESeq2. *Genome Biol* **15**, 550 (2014).
1174 <https://doi.org/10.1186/s13059-014-0550-8>

1175 97 Benjamini, Y. & Hochberg, Y. Controlling the false discovery rate: a practical
1176 and powerful approach to multiple testing. *Journal of the Royal statistical
1177 society: series B (Methodological)* **57**, 289-300 (1995).

1178 98 Wu, T. *et al.* clusterProfiler 4.0: A universal enrichment tool for interpreting
1179 omics data. *Innovation (Camb)* **2**, 100141 (2021).
1180 <https://doi.org/10.1016/j.xinn.2021.100141>

1181 99 Conway, J. R., Lex, A. & Gehlenborg, N. UpSetR: an R package for the
1182 visualization of intersecting sets and their properties. *Bioinformatics* **33**, 2938-
1183 2940 (2017). <https://doi.org/10.1093/bioinformatics/btx364>

1184 100 Blighe, K., Rana, S. & Lewis, M. *EnhancedVolcano: Publication-ready volcano
1185 plots with enhanced colouring and labeling.* (2022).

1186 101 Chen, H. & Boutros, P. C. VennDiagram: a package for the generation of highly-
1187 customizable Venn and Euler diagrams in R. *BMC Bioinformatics* **12**, 35 (2011).
1188 <https://doi.org/10.1186/1471-2105-12-35>

1189 102 Blake, J. A. *et al.* Mouse Genome Database (MGD): Knowledgebase for
1190 mouse-human comparative biology. *Nucleic Acids Res* **49**, D981-D987 (2021).
1191 <https://doi.org/10.1093/nar/gkaa1083>

1192 103 Seal, R. L. *et al.* Genenames.org: the HGNC resources in 2023. *Nucleic Acids
1193 Res* **51**, D1003-D1009 (2023). <https://doi.org/10.1093/nar/gkac888>

1194 104 Pedregosa, F. *et al.* Scikit-learn: Machine learning in Python. *the Journal of
1195 machine Learning research* **12**, 2825-2830 (2011).

1196 105 Granja, J. M. *et al.* ArchR is a scalable software package for integrative single-
1197 cell chromatin accessibility analysis. *Nat Genet* **53**, 403-411 (2021).
1198 <https://doi.org/10.1038/s41588-021-00790-6>

1199 106 Zhang, Y. *et al.* Model-based analysis of ChIP-Seq (MACS). *Genome Biol* **9**,
1200 R137 (2008). <https://doi.org/10.1186/gb-2008-9-9-r137>

1201 107 Stuart, T., Srivastava, A., Madad, S., Lareau, C. A. & Satija, R. Single-cell
1202 chromatin state analysis with Signac. *Nat Methods* **18**, 1333-1341 (2021).
1203 <https://doi.org/10.1038/s41592-021-01282-5>

1204 108 Robinson, M. D., McCarthy, D. J. & Smyth, G. K. edgeR: a Bioconductor
1205 package for differential expression analysis of digital gene expression data.
1206 *Bioinformatics* **26**, 139-140 (2010).
1207 <https://doi.org/10.1093/bioinformatics/btp616>

1208 109 Hoffman, G. E. & Schadt, E. E. variancePartition: interpreting drivers of
1209 variation in complex gene expression studies. *BMC Bioinformatics* **17**, 483
1210 (2016). <https://doi.org/10.1186/s12859-016-1323-z>

1211 110 Lehallier, B. *et al.* Undulating changes in human plasma proteome profiles
1212 across the lifespan. *Nat Med* **25**, 1843-1850 (2019).
<https://doi.org/10.1038/s41591-019-0673-2>

1213 111 Murphy, A. E., Schilder, B. M. & Skene, N. G. MungeSumstats: a Bioconductor
1214 package for the standardization and quality control of many GWAS summary
1215 statistics. *Bioinformatics* **37**, 4593-4596 (2021).
<https://doi.org/10.1093/bioinformatics/btab665>

1216 112 Skene, N. G. & Grant, S. G. Identification of Vulnerable Cell Types in Major
1217 Brain Disorders Using Single Cell Transcriptomes and Expression Weighted
1218 Cell Type Enrichment. *Front Neurosci* **10**, 16 (2016).
<https://doi.org/10.3389/fnins.2016.00016>

1219 113 Wang, G., Sarkar, A., Carbonetto, P. & Stephens, M. A simple new approach
1220 to variable selection in regression, with application to genetic fine mapping. *J R
1221 Stat Soc Series B Stat Methodol* **82**, 1273-1300 (2020).
<https://doi.org/10.1111/rssb.12388>

1222 114 Wallace, C. A more accurate method for colocalisation analysis allowing for
1223 multiple causal variants. *PLoS Genet* **17**, e1009440 (2021).
<https://doi.org/10.1371/journal.pgen.1009440>

1224 115 Coetzee, S. G., Coetzee, G. A. & Hazelett, D. J. motifbreakR: an
1225 R/Bioconductor package for predicting variant effects at transcription factor
1226 binding sites. *Bioinformatics* **31**, 3847-3849 (2015).
<https://doi.org/10.1093/bioinformatics/btv470>

1227 116 Grissa, D., Junge, A., Oprea, T. I. & Jensen, L. J. Diseases 2.0: a weekly
1228 updated database of disease-gene associations from text mining and data
1229 integration. *Database (Oxford)* **2022** (2022).
<https://doi.org/10.1093/database/baac019>

1230
1231
1232
1233
1234
1235
1236
1237
1238

1239 **Figure legends**

1240

1241 **Figure 1. Overview of single cell atlas of the human retina**

1242 A. The integrated study for the atlas involves compiling public datasets and in-house
1243 generated data, integrating datasets, annotating cell clusters, utilizing chromatin profiles for
1244 multi-omics, and demonstrating the utility by applications. B. Collected retinal datasets
1245 comprising of both in-house newly generated and seven publicly available datasets. C. Five
1246 data integration algorithms are benchmarked for data harmonization. The algorithms are
1247 evaluated using 14 metrics, with the rows representing the algorithms and columns
1248 corresponding to the metrics. The algorithms are ranked based on their overall score. D. The
1249 atlas of snRNA-seq datasets is visualized in a UMAP plot at a major class resolution, with
1250 cells colored based on their major classes. E. Cell type similarities of major classes between
1251 snRNA-seq (in coral) and scRNA-seq (in blue). The color key is the average AUROC of self-
1252 projection for cell types. F. Volcano plot of genes over-expressed in snRNA-seq datasets (on
1253 the right) and scRNA-seq (on the left). The x-axis is log2 fold change, and the y-axis is $-\log_{10}$
1254 q -value. Differentially expressed genes were identified under \log_{10} fold change >1 and q -
1255 value <0.05 and are depicted as red dots. Selected gene symbols point to the DEGs, including
1256 seven genes encoding protocadherin proteins on the right: *PCDHGB2*, *PCDHGB3*, *PCDHGB4*,
1257 *PCDHGA2*, *PCDHA2*, *PCDHGA11*, *PCDHA8*; and five genes encoding ribosomal proteins on
1258 the left: *RPL7*, *RPL13A*, *RPS8*, *RPS15*, *RPS17*.

1259

1260 **Figure 2. Bipolar cells**

1261 A. Distribution of marker genes for BC types. BC subclasses are in RB, OFF and ON. NETO1,
1262 OTX2, and VSX2 were used as BC pan-markers. GRIK1 and GRM6 were used as OFF and
1263 ON markers, respectively. Rows represent marker genes, and columns represent BC types.
1264 The names of BC types are extracted from macaque BC types. B. UMAP visualization of
1265 human BC cells. Cell clusters are colored by the annotated cell types. C. Co-embedding of
1266 human, mouse, and macaque BC cells. To differentiate between cell types from three species,
1267 prefixes were added to the names: “h” for human, “m” for mouse, and “a” for macaque. D.
1268 Hierarchical clustering of mouse BC cell types. Expanded leaf nodes are the correspondent
1269 cell types from human and macaque BC cell types. E. The overlap between the top-ranked
1270 genes of human GB and BB is examined using snRNA-seq and scRNA-seq datasets. Fisher’s
1271 exact test was used to calculate the significance of the overlap of top ranked genes in GB (p -
1272 value= 7.5×10^{-293}) and BB (p -value= 1.7×10^{-131}) between snRNA-seq and scRNA-seq. F. Cell

1273 type similarities among mouse BC5A, BC5B, BC5C, and BC5D, and mapped types in humans
1274 and macaques.

1275

1276 **Figure 3. Amacrine cells and retinal ganglion cells**

1277 A. UMAP visualization of the identified 73 AC cell clusters. Cluster IDs are placed on top of
1278 clusters, and cells are colored by the cluster IDs, where 14 clusters have annotated types. B.
1279 Dot plot of predicted markers for AC cell types. C. UMAP visualization of RGC cell types with
1280 labels on top of cells. D. Sankey diagram illustrating RGC types alignment between humans
1281 (left column) and macaques (right column). E. Dot plot of predicted markers for RGC cell types.
1282

1283 **Figure 4. A high resolution snATAC-seq cell atlas of the human retina**

1284 A. Uniform Manifold Approximation and Projection (UMAP) of co-embedded cells from
1285 snRNA-seq and snATAC-seq showing cells are clustered into major retinal cell classes. B. Pie
1286 chart showing the cell proportion distribution of major retinal cell classes in this study. C. Dot
1287 plot showing marker gene expression measured by snRNA-seq and marker gene activity
1288 score derived from snATAC-seq are specific in the corresponding cell class. D. Bar plot
1289 showing the number of open chromatin regions (OCRs) identified in each major cell class. E.
1290 The Venn Diagram showing the overlapped OCRs detected by retinal snATAC-seq and bulk
1291 ATAC-seq. F. Pie chart showing cell type specificity of OCRs identified from retinal snATAC-
1292 seq (left) and bulk ATAC-seq (right). The color codes the number of cell types where the OCRs
1293 were observed. G. Heatmap showing chromatin accessibility (left) and gene expression (right)
1294 of 149,273 significantly linked CRE-gene pairs identified by the correlation between gene
1295 expression and OCR accessibility. Rows represented CRE-gene pairs grouped in clusters by
1296 correlations. H. Volcano plot showing the \log_2FC value (comparison between activity of each
1297 tested sequence and the activity of a basal CRX promoter, X axis) and the $-\log_{10}FDR$ value
1298 (Y axis) of each tested sequence by MPRAs (IRD CREs n=1,820, control CREs with a variety
1299 of activities n=20, Scrambled CREs n=300). Each dot corresponds to a tested sequence,
1300 colored by the activity of the sequence. I. Scatter plot showing the eRegulon specificity score
1301 for each transcription factor (TF) and the corresponding regulon across major retinal cell
1302 classes. The top five TF and eRegulon are highlighted in red.

1303

1304 **Figure 5. Regulon of the human bipolar cell types**

1305 A. Heatmap showing the identified regulons where the gene expression level (color scale) of
1306 transcription factors and the enrichment (dot size) of TF motifs in the snATAC peaks are highly
1307 correlated. The rows represent BC cell types, and the columns represent the identified

1308 regulons. B. Jaccard heatmap showing the intersection of target regions of the identified TFs.
1309 Each cell in the heatmap represents the Jaccard index of target regions between a pair of TFs.
1310 C. Jaccard heatmap showing the intersection of target genes of the identified TFs. Each cell
1311 in the heatmap represents the Jaccard index of target genes between a pair of TFs. D.
1312 Network plot showing the regulons and interactions between them in DB3a, DB3b, BB and
1313 GB. Each regulon includes the TF, target regions and target genes. E. ROC-AUC of logistic
1314 regression model and SVM model to predict BC cell type based on the accessibility of target
1315 regions of identified TFs. F. Heatmap showing the correlation in target-regions-based AUC of
1316 the identified regulons.

1317

1318 **Figure 6. Differential gene expression associated with sex and age.**

1319 A. Heatmap showing gene expression level of differentially expressed genes (DEGs) during
1320 aging in Rod identified with linear mixed effect model (LMM). B. UpSet plot showing the
1321 number of cell type specific and common DEGs across major retinal cell classes. C. The
1322 number of DEGs identified through sliding window analysis at each age stage. D. The selected
1323 KEGG pathways significantly enriched (FDR <0.1) of DEGs during aging identified by LMM
1324 across retinal cell classes. E. The examples of DEG during aging involved in the enriched
1325 KEGG pathways. F. The number of DEGs between male and female across major retinal cell
1326 classes. G. The selected GO terms significantly enriched (FDR < 0.1) of DEGs between male
1327 and female across retinal cell classes. H. The selected KEGG pathways significantly enriched
1328 (FDR < 0.1) of DEGs with gender dependent aging effect. I. The examples of DEGs with
1329 gender dependent aging effect involved in the enriched KEGG pathways.

1330

1331 **Figure 7. Leveraging multi-omics data to study GWAS and eQTL loci**

1332 A. Cell class enrichment of GWAS loci based on chromatin accessibility with LDSC (left) and
1333 gene expression with MAGMA (right). Rows represent enriched GWAS traits, and columns
1334 represent retinal cell classes. The highlight dot indicates the enrichment q-value < 0.05. B.
1335 Categorization of fine-mapped GWAS variants located in various genomic regions. Categories
1336 include peak (i.e., open chromatin regions), linked cis-regulatory elements (CREs),
1337 differentially accessible regions (DARs), promoter, exon, 5_UTR and 3_UTR of gene
1338 annotation. C. Categorization of fine-mapped eQTL variants located in various genomic
1339 regions. D. Visualization of fine-mapped loci in *CLIC5* region.

1340

1341 **Extended Data Figure legends**

1342

1343 **Extended Data Figure 1. Overview of the HRCA.**

1344 A. Cell proportion distribution of major classes among donors. The x-axis corresponds to each
1345 donor, and the y-axis is the cell proportion of major classes. The last bar is the cell proportion
1346 across total cells. B. A pie chart illustrating the number of cells for major classes and their
1347 proportions. C. Integration of datasets from snRNA-seq and scRNA-seq datasets. The cells
1348 are colored by major classes. D. The atlas is colored by the two technologies: snRNA-seq (in
1349 coral) and scRNA-seq (in blue). E. The distribution of transcriptomic data for 152 samples
1350 obtained from snRNA-seq and scRNA-seq technologies. Each sample is colored by the
1351 technology used. F. The atlas of scRNA-seq data, with major classes represented using
1352 different colors. G. Dot plots illustrating the distribution of expression levels of marker genes
1353 for major cell classes in snRNA-seq (on the left) and scRNA-seq data (on the right).

1354

1355 **Extended Data Figure 2. Comparison between single-nuclei and single-cell
1356 technologies.**

1357 A. Cell proportion of major class of samples between snRNA-seq and scRNA-seq in fovea,
1358 macular, and periphery tissue regions. The red bar represents cell proportions of major
1359 classes in snRNA-seq samples, and the blue bar represents cell proportions of scRNA-seq
1360 samples. B. Enriched GO BPs of 1,387 over-expressed genes in snRNA-seq data. C.
1361 Enriched GO BPs of 3,242 over-expressed genes in scRNA-seq data. D. Shared genes over-
1362 expressed in snRNA-seq data among major cell classes. The "Full" (in red) is genes over-
1363 expressed in snRNA-seq data regardless of cell classes. E. Shared of genes derived from
1364 scRNA-seq data.

1365

1366 **Extended Data Figure 3. transcriptomic signature of bipolar cells**

1367 A. UMAP visualization of BC cells based on single-cell transcriptome data. B. Dot plot of the
1368 distribution of marker gene expression by the single-cell measurements. C. Co-embedding
1369 between snRNA-seq and scRNA-seq cells. The label names are prefixed by "n" for snRNA
1370 and "c" for scRNA. D. Volcano plot of differentially expressed genes between GB and BB of
1371 the snRNA-seq datasets. Differentially expressed genes were identified under \log_2 fold
1372 change >1 and $q\text{-value} < 0.05$. E. Predicted markers per BC cell type by the binary classification
1373 analysis using snRNA-seq datasets. Rows are BC cell types, and columns represent novel
1374 markers.

1375

1376

1377 **Extended Data Figure 4. Annotation of amacrine cells.**

1378 A. Dot plot of AC cell clusters by markers to identify AC subclasses for GABAergic, Glycinergic,
1379 and Both. *PAX6* and *TFAP2B* were used as AC pan-markers. *GAD1/GAD2* were used for
1380 GABAergic ACs, and *SLC6A9* was used for the Glycinergic ACs. *MEIS2*, *TCF4*, and *EBF1*
1381 were also included in the dot plot. B. UMAP of AC cells, colored by the four AC groups. C. Dot
1382 plot of 14 AC cell clusters with known markers. The cell type names are indicated in
1383 parentheses next to the cluster IDs. D. UMAP visualization of AC cells, colored by the 14
1384 clusters with cell type names. The rest of the clusters are colored as “unknown” without
1385 existing names.

1386

1387 **Extended Data Figure 5. Cross-mapping for human amacrine cells.**

1388 A. SATURN co-embedding visualization of AC cell types between snRNA-seq and scRNA-
1389 seq. AC cells are colored by the two technologies. B. The same SATURN co-embedding with
1390 AC type labels color-coded on top of clusters. Labels are prefixed with “n” for snRNA-seq
1391 datasets and “c” for scRNA-seq data. C. SATURN co-embedding visualization of AC types
1392 across human, macaque and mouse species. AC cell labels for the three species are overlaid
1393 on clusters. Labels are prefixed with “h” for human, “a” for macaque, and “m” for mouse.

1394

1395 **Extended Data Figure 6. Annotation of retinal ganglion cells.**

1396 A. Dot plot of RGC cell clusters with existing markers. B. The proportion of parasol RGCs
1397 within the RGC population in the samples. Samples enriched by NeuN experiments are
1398 highlighted in green. C. Sankey diagram depicting the relationship between RGC clusters from
1399 snRNA-seq datasets and the public labeling of RGC types from scRNA-seq datasets. The
1400 width of the lines is proportional to the number of cells in the mapping. D. Sankey diagram
1401 illustrating RGC types alignment between humans (left column) and mice (right column).

1402

1403 **Extended Data Figure 7. A high resolution snATAC-seq cell atlas of the human retina**

1404 A. Scatter plot showing the correlation between gene expression derived from snRNA-seq (X
1405 axis) and gene activity score derived from snATAC-seq (Y axis) from major retinal cell classes.
1406 B. Heatmap showing the chromatin accessibility of differential accessible regions (DARs)
1407 identified in major retinal cell classes. Rows represented chromatin regions specific to certain
1408 major classes, and columns corresponded to major classes. C. Genome track of the *RHO*
1409 locus showing the cell type specific chromatin accessibility in the promoter and linked cis-
1410 regulatory elements of this gene. D. Density plot showing the activity (log₂FC value of

1411 comparison between activity of each tested sequence and the activity of a basal CRX promoter)
1412 distribution of the tested sequences by MPRA. IRD CREs n=1,820 (green), control CREs
1413 with a variety of activities n=20 (red), Scrambled CREs n=300 (blue).

1414

1415 **Extended Data Figure 8. Multi-omics atlas of the human retinal subclass cell types**

1416 A. UMAP showing the co-embedding of bipolar cells (BC) from snRNA-seq and snATAC-seq
1417 were clustered into BC cell types. B. Dot plot showing marker gene expression measured by
1418 snRNA-seq and marker gene activity score derived from snATAC-seq are specific in the
1419 corresponding BC cell types. C. Genome track of SORCS3 showing the promoter of SORCS3
1420 is specifically open in BB. D. Genome track of UTRN showing the local chromatin of UTRN is
1421 specifically open in GB. E. UMAP showing the co-embedding of amacrine cells (AC) from
1422 snRNA-seq and snATAC-seq were clustered into AC cell types. F. Dot plot showing marker
1423 gene expression measured by snRNA-seq and marker gene activity score derived from
1424 snATAC-seq are specific in the corresponding sub classes of AC types. G. UMAP showing
1425 the co-embedding of cone cells (Cone) from snRNA-seq and snATAC-seq were clustered in
1426 Cone cell types. H. Dot plot showing marker gene expression measured by snRNA-seq and
1427 marker gene activity score derived from snATAC-seq are specific in the corresponding Cone
1428 cell types.

1429

1430 **Extended Data Figure 9. Regulon of the human retinal subclass cell types**

1431 A. Dot plot showing the distribution of regulon specificity score of regulons identified in ML-
1432 and S-Cone. B. Dot plot showing the distribution of regulon specificity score of regulons
1433 identified in OFF- and ON-BC (ON-BC include ON-Cone BC and Rod BC). C. Dot plot showing
1434 the distribution of regulon specificity score of regulons identified in GABAergic-, Glycinergic-
1435 and Both-AC. D. Dot plot showing the distribution of regulon specificity score of regulons
1436 identified in HC0 and HC1. E. Dot plot showing the distribution of regulon specificity score of
1437 regulons identified in 14 BC cell types. F. Boxplot showing the average AUC values of the
1438 regulon modules identified in BC cell types. The BC cell types with the highest AUC values
1439 were labeled in the title of each regulon module.

1440

1441 **Extended Data Figure 10. Differential gene expression during aging and associated with**
1442 **sex.**

1443 A. Age and sex distribution of the analyzed samples. B. Heatmap showing gene expression
1444 level of differentially expressed genes (DEGs) during aging in major retinal cell classes
1445 identified with linear mixed effect model (LMM). C. UpSet plot showing the overlap of DEGs

1446 identified by LMM and sliding-window analysis at the age of 30, 60 and 80 in Rod. UpSet plot
1447 showing the number of DEGs across major retinal cell classes at the age of 30, 60 and 80,
1448 respectively. D. The GO terms significantly enriched (FDR <0.1) of DEGs during aging
1449 identified by LMM across retinal cell classes. E. The examples of DEGs between male and
1450 female associated with the enriched GO terms.

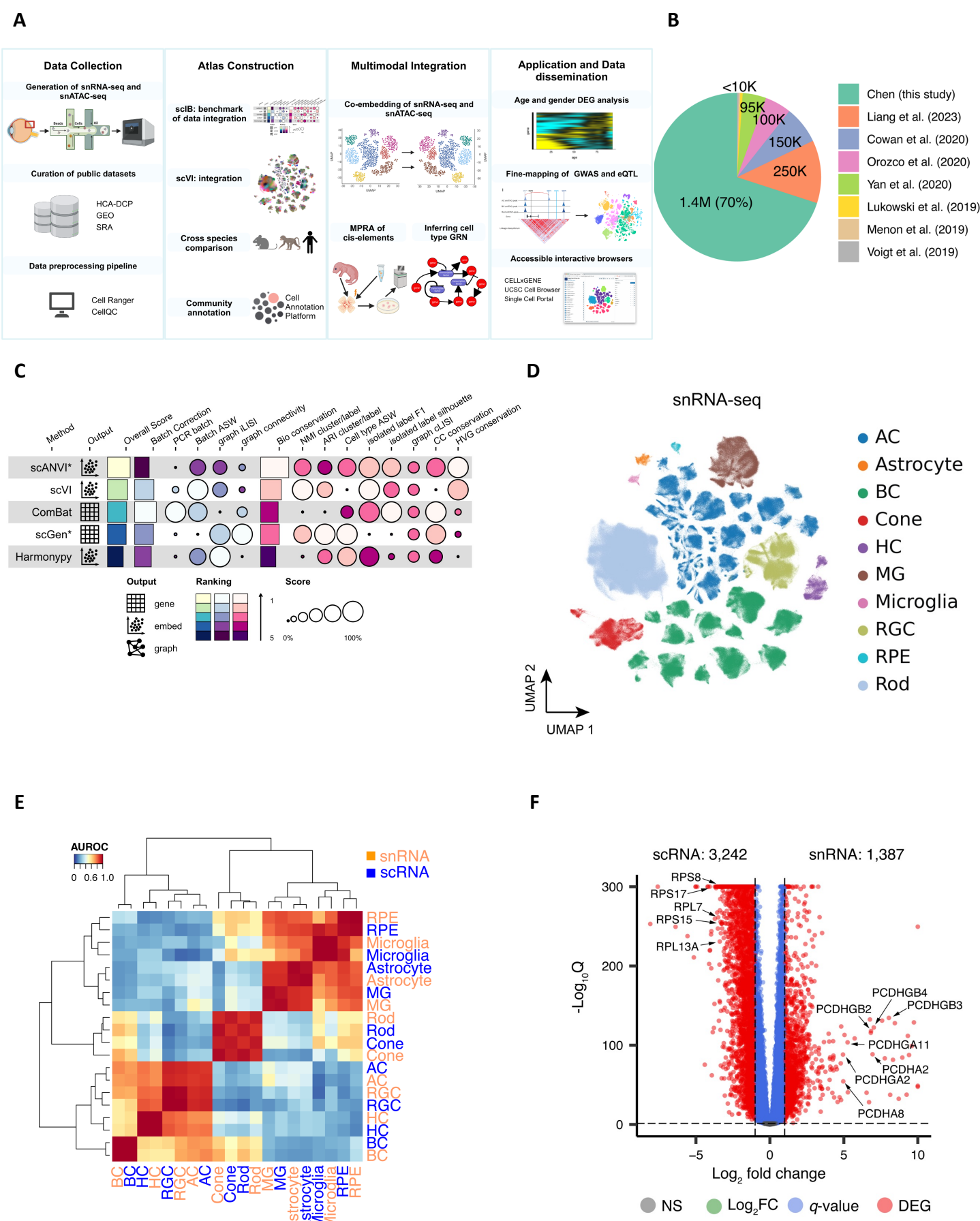


Figure 1. Overview of single cell atlas of the human retina

Figure 1. Overview of single cell atlas of the human retina

A. The integrated study for the atlas involves compiling public datasets and in-house generated data, integrating datasets, annotating cell clusters, utilizing chromatin profiles for multi-omics, and demonstrating the utility by applications. B. Collected retinal datasets comprising of both in-house newly generated and seven publicly available datasets. C. Five data integration algorithms are benchmarked for data harmonization. The algorithms are evaluated using 14 metrics, with the rows representing the algorithms and columns corresponding to the metrics. The algorithms are ranked based on their overall score. D. The atlas of snRNA-seq datasets is visualized in a UMAP plot at a major class resolution, with cells colored based on their major classes. E. Cell type similarities of major classes between snRNA-seq (in coral) and scRNA-seq (in blue). The color key is the average AUROC of self-projection for cell types. F. Volcano plot of genes over-expressed in snRNA-seq datasets (on the right) and scRNA-seq (on the left). The x-axis is log2 fold change, and the y-axis is $-\log_{10} q\text{-value}$. Differentially expressed genes were identified under $|\log_2 \text{fold change}| > 1$ and $q\text{-value} < 0.05$ and are depicted as red dots. Selected gene symbols point to the DEGs, including seven genes encoding protocadherin proteins on the right: *PCDHGB2*, *PCDHGB3*, *PCDHGB4*, *PCDHGA2*, *PCDHA2*, *PCDHGA11*, *PCDHA8*; and five genes encoding ribosomal proteins on the left: *RPL7*, *RPL13A*, *RPS8*, *RPS15*, *RPS17*.

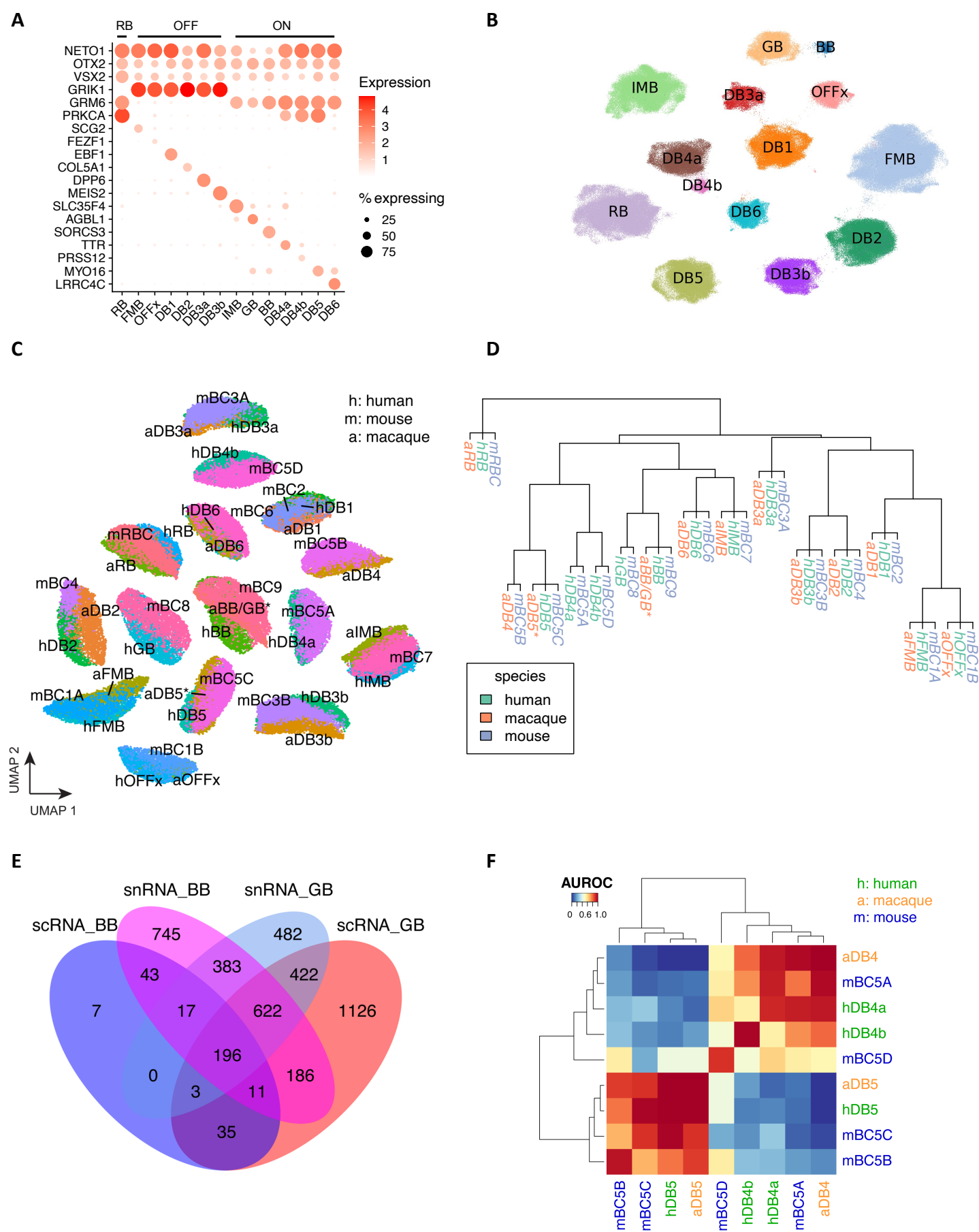
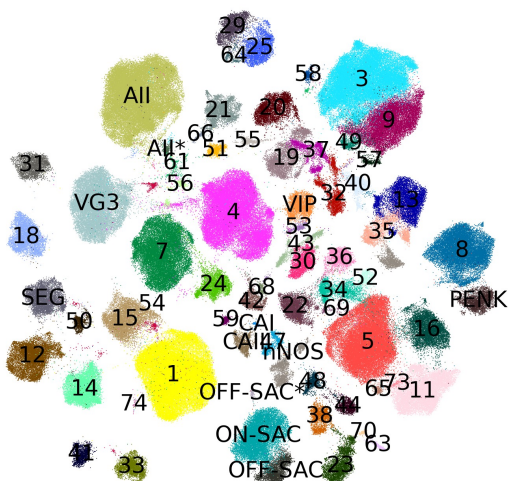


Figure 2. Bipolar cells

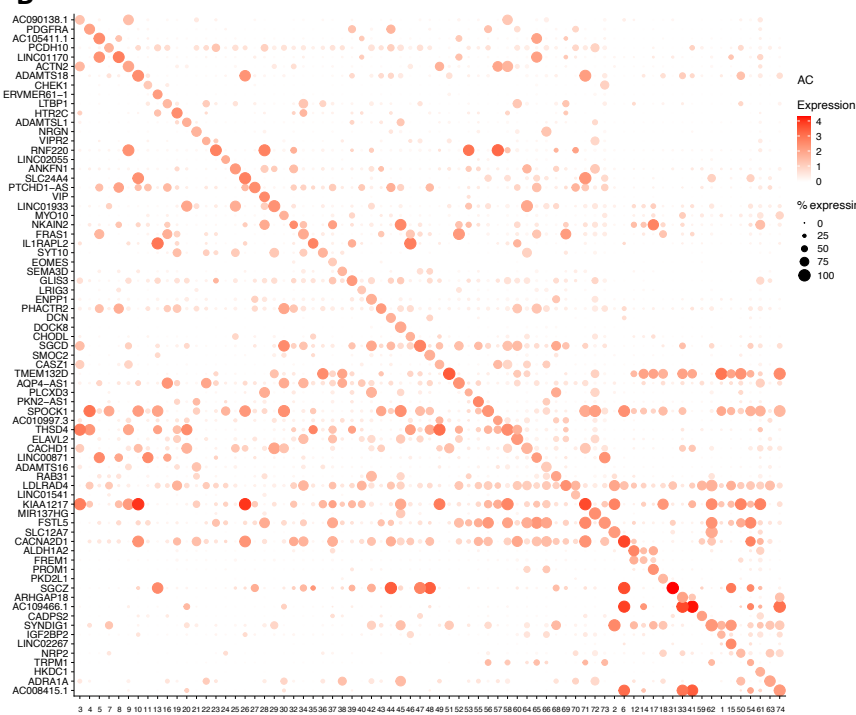
Figure 2. Bipolar cells

A. Distribution of marker genes for BC types. BC subclasses are in RB, OFF and ON. NETO1, OTX2, and VSX2 were used as BC pan-markers. GRIK1 and GRM6 were used as OFF and ON markers, respectively. Rows represent marker genes, and columns represent BC types. The names of BC types are extracted from macaque BC types. B. UMAP visualization of human BC cells. Cell clusters are colored by the annotated cell types. C. Co-embedding of human, mouse, and macaque BC cells. To differentiate between cell types from three species, prefixes were added to the names: "h" for human, "m" for mouse, and "a" for macaque. D. Hierarchical clustering of mouse BC cell types. Expanded leaf nodes are the correspondent cell types from human and macaque BC cell types. E. The overlap between the top-ranked genes of human GB and BB is examined using snRNA-seq and scRNA-seq datasets. Fisher's exact test was used to calculate the significance of the overlap of top ranked genes in GB ($p\text{-value}=7.5\times10^{-293}$) and BB ($p\text{-value}=1.7\times10^{-131}$) between snRNA-seq and scRNA-seq. F. Cell type similarities among mouse BC5A, BC5B, BC5C, and BC5D, and mapped types in humans and macaques.

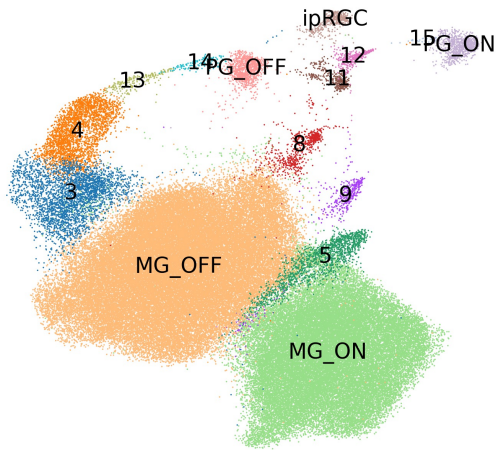
A



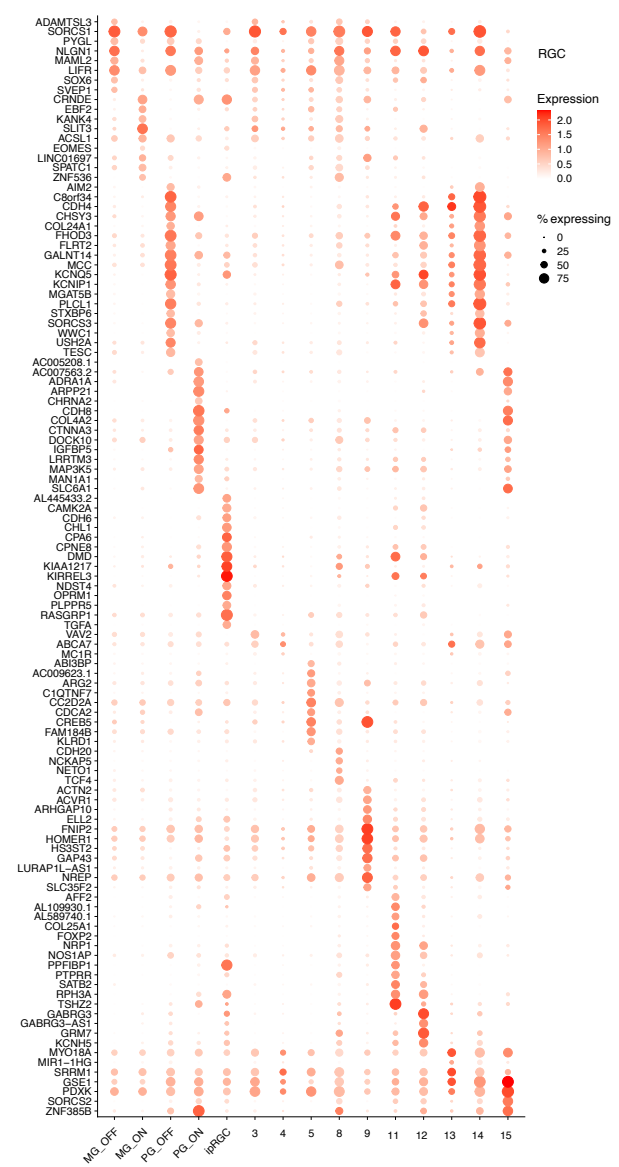
B



C



E



D

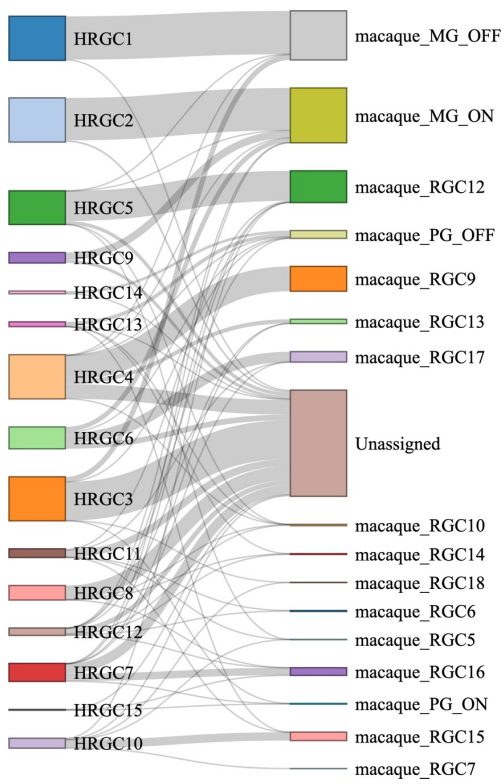


Figure 3. Amacrine cells and retinal ganglion cells

Figure 3. Amacrine cells and retinal ganglion cells

A. UMAP visualization of the identified 73 AC cell clusters. Cluster IDs are placed on top of clusters, and cells are colored by the cluster IDs, where 14 clusters have annotated types. B. Dot plot of predicted markers for AC cell types. C. UMAP visualization of RGC cell types with labels on top of cells. D. Sankey diagram illustrating RGC types alignment between humans (left column) and macaques (right column). E. Dot plot of predicted markers for RGC cell types.



Figure 4. A high resolution snATAC-seq cell atlas of the human retina

Figure 4. A high resolution snATAC-seq cell atlas of the human retina

A. Uniform Manifold Approximation and Projection (UMAP) of co-embedded cells from snRNA-seq and snATAC-seq showing cells are clustered into major retinal cell classes. B. Pie chart showing the cell proportion distribution of major retinal cell classes in this study. C. Dot plot showing marker gene expression measured by snRNA-seq and marker gene activity score derived from snATAC-seq are specific in the corresponding cell class. D. Bar plot showing the number of open chromatin regions (OCRs) identified in each major cell class. E. The Venn Diagram showing the overlapped OCRs detected by retinal snATAC-seq and bulk ATAC-seq. F. Pie chart showing cell type specificity of OCRs identified from retinal snATAC-seq (left) and bulk ATAC-seq (right). The color codes the number of cell types where the OCRs were observed. G. Heatmap showing chromatin accessibility (left) and gene expression (right) of 149,273 significantly linked CRE-gene pairs identified by the correlation between gene expression and OCR accessibility. Rows represented CRE-gene pairs grouped in clusters by correlations. H. Volcano plot showing the \log_2FC value (comparison between activity of each tested sequence and the activity of a basal CRX promoter, X axis) and the $-\log_{10}FDR$ value (Y axis) of each tested sequence by MPRAs (IRD CREs n=1,820, control CREs with a variety of activities n=20, Scrambled CREs n=300). Each dot corresponds to a tested sequence, colored by the activity of the sequence. I. Scatter plot showing the eRegulon specificity score for each transcription factor (TF) and the corresponding regulon across major retinal cell classes. The top five TF and eRegulon are highlighted in red.

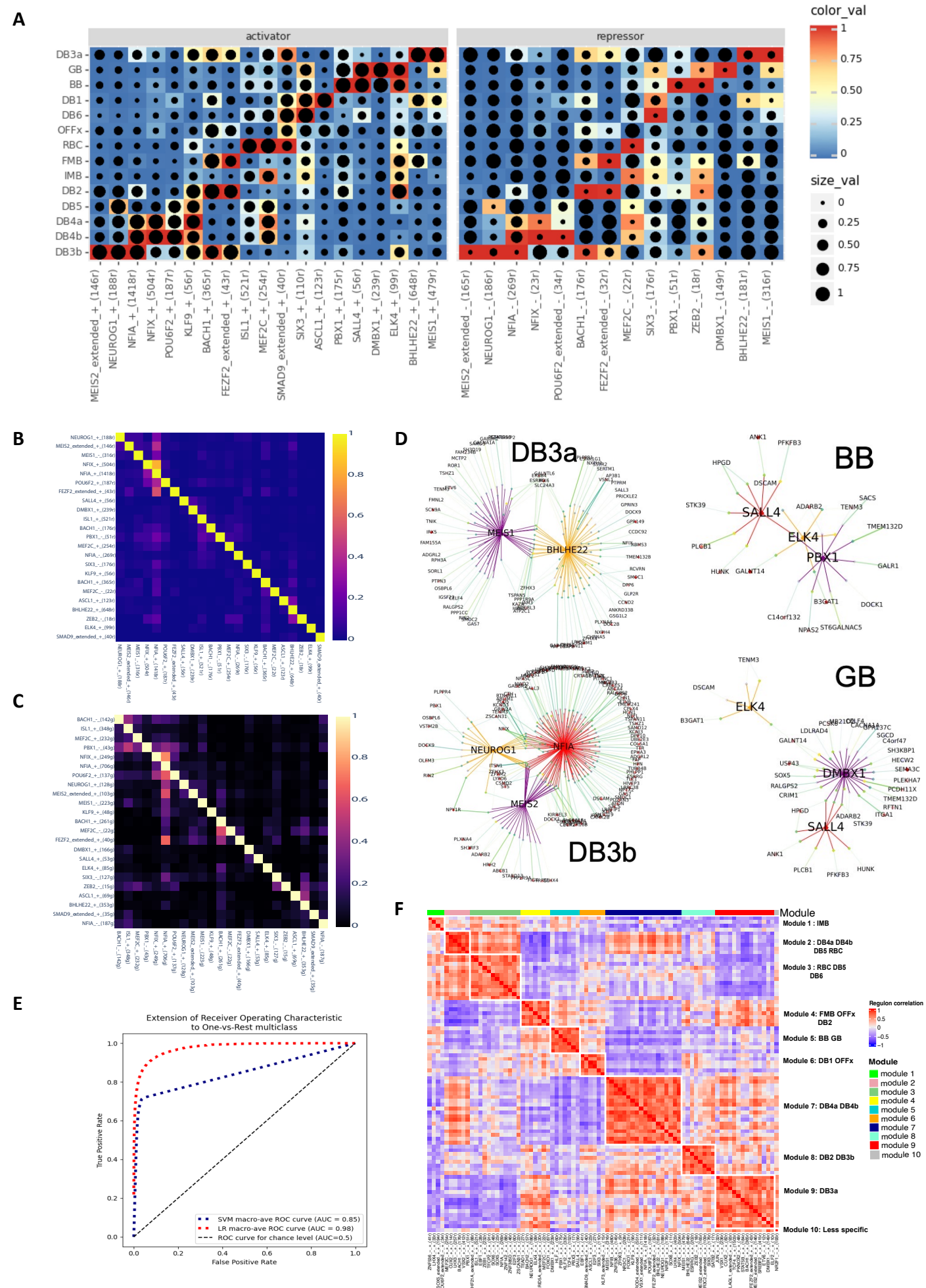


Figure 5. Regulon of the human bipolar cell types

Figure 5. Regulon of the human bipolar cell types

A. Heatmap showing the identified regulons where the gene expression level (color scale) of transcription factors and the enrichment (dot size) of TF motifs in the snATAC peaks are highly correlated. The rows represent BC cell types, and the columns represent the identified regulons. B. Jaccard heatmap showing the intersection of target regions of the identified TFs. Each cell in the heatmap represents the Jaccard index of target regions between a pair of TFs. C. Jaccard heatmap showing the intersection of target genes of the identified TFs. Each cell in the heatmap represents the Jaccard index of target genes between a pair of TFs. D. Network plot showing the regulons and interactions between them in DB3a, DB3b, BB and GB. Each regulon includes the TF, target regions and target genes. E. ROC-AUC of logistic regression model and SVM model to predict BC cell type based on the accessibility of target regions of identified TFs. F. Heatmap showing the correlation in target-regions-based AUC of the identified regulons.

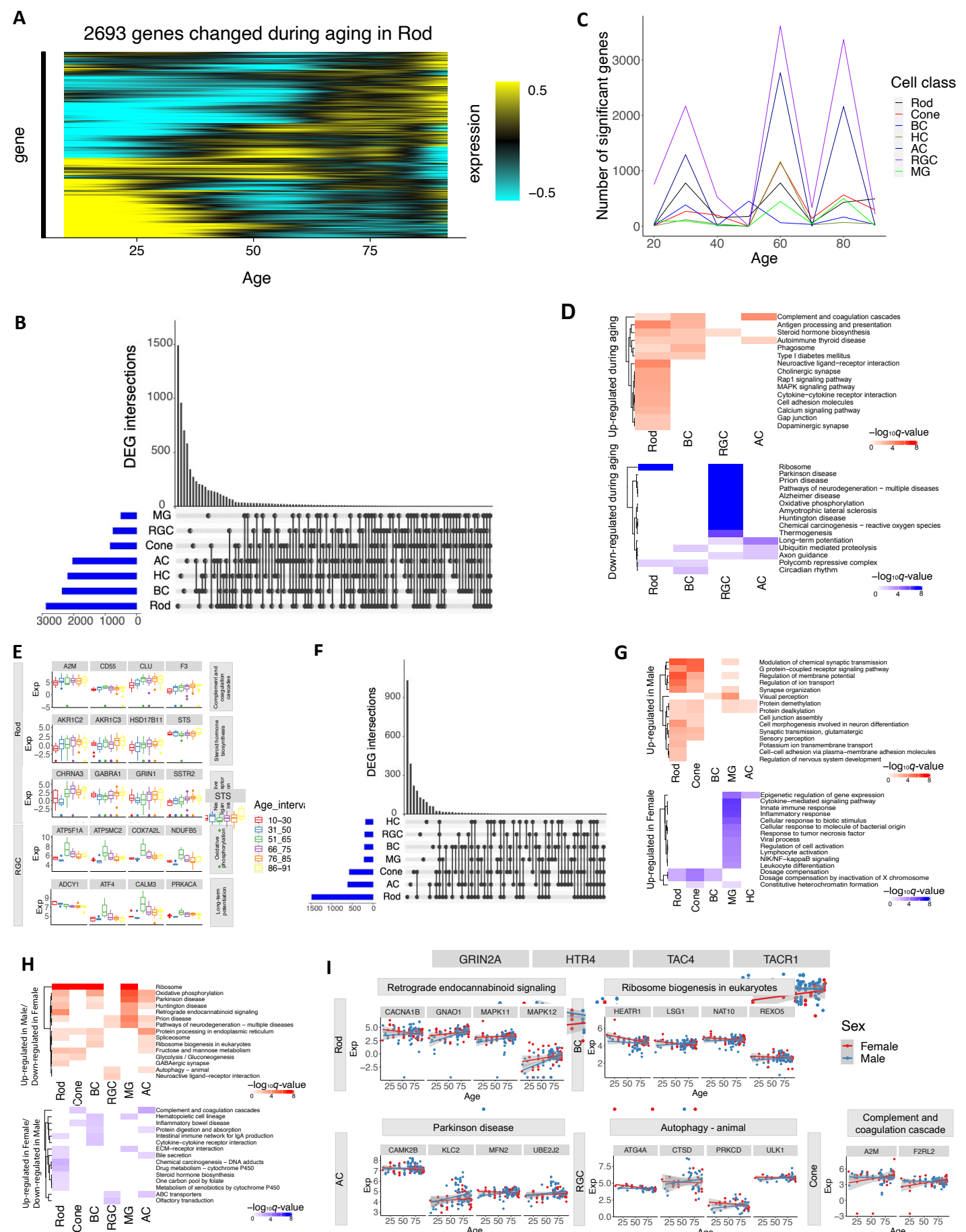


Figure 6. Differential gene expression during aging and associated with sex.

Figure 6. Differential gene expression associated with age and sex.

A. Heatmap showing gene expression level of differentially expressed genes (DEGs) during aging in Rod identified with linear mixed effect model (LMM). B. UpSet plot showing the number of cell type specific and common DEGs across major retinal cell classes. C. The number of DEGs identified through sliding window analysis at each age stage. D. The selected KEGG pathways significantly enriched (FDR < 0.1) of DEGs during aging identified by LMM across retinal cell classes. E. The examples of DEG during aging involved in the enriched KEGG pathways. F. The number of DEGs between male and female across major retinal cell classes. G. The selected GO terms significantly enriched (FDR < 0.1) of DEGs between male and female across retinal cell classes. H. The selected KEGG pathways significantly enriched (FDR < 0.1) of DEGs with gender dependent aging effect. I. The examples of DEGs with gender dependent aging effect involved in the enriched KEGG pathways.

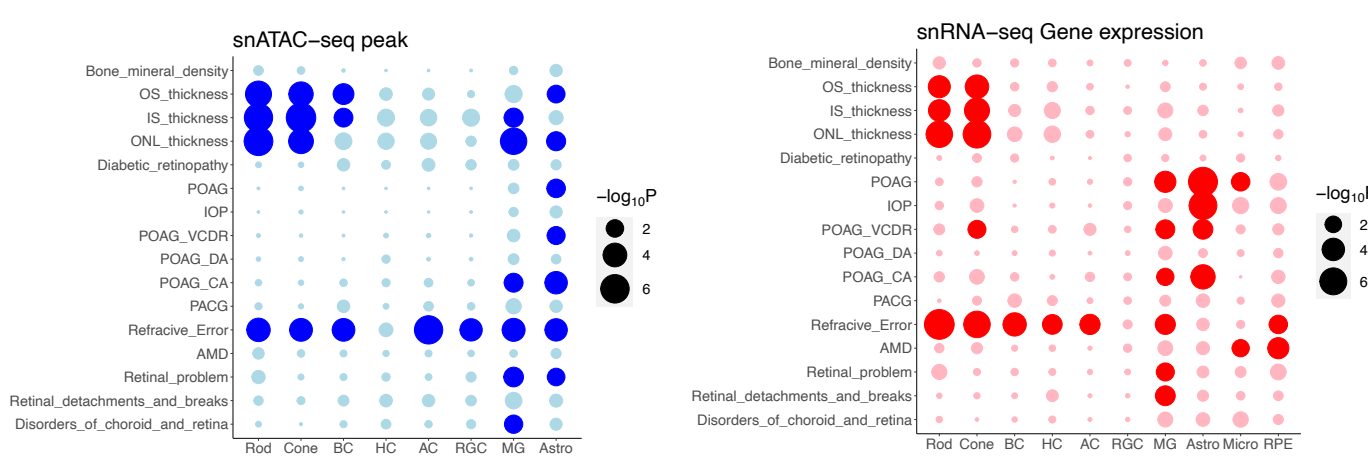
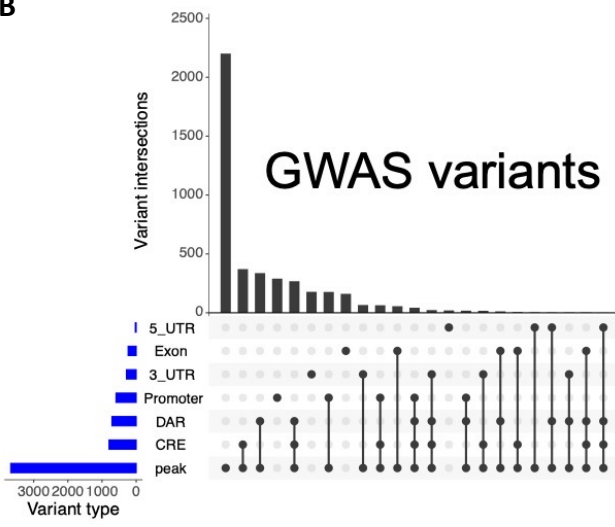
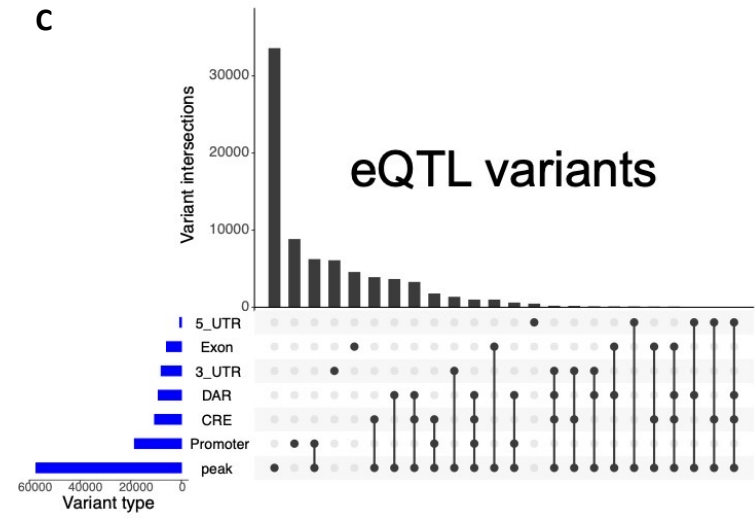
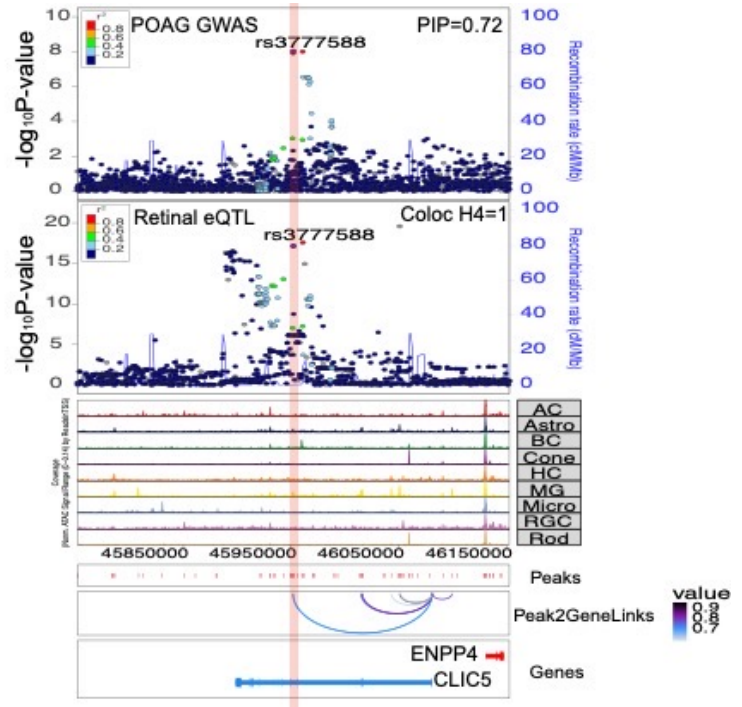
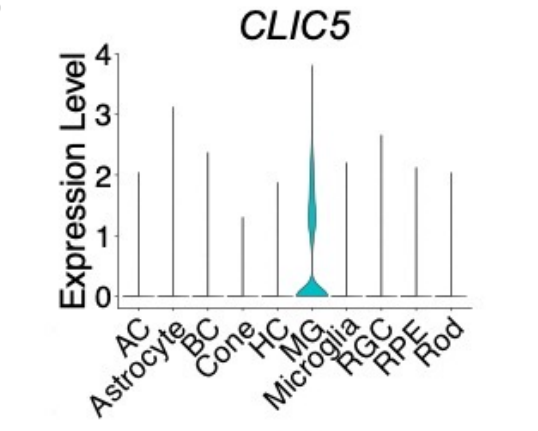
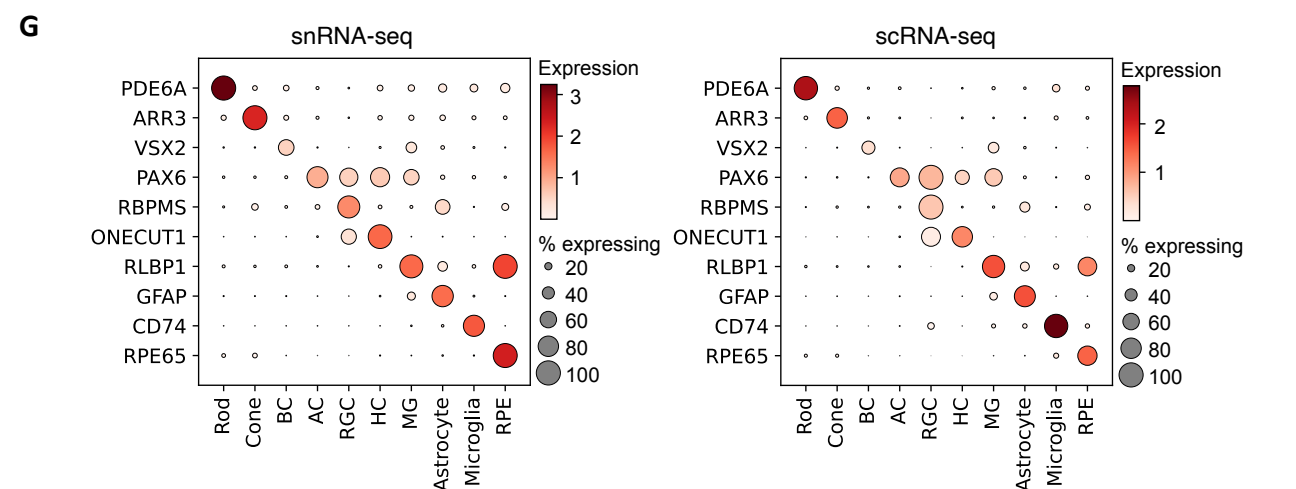
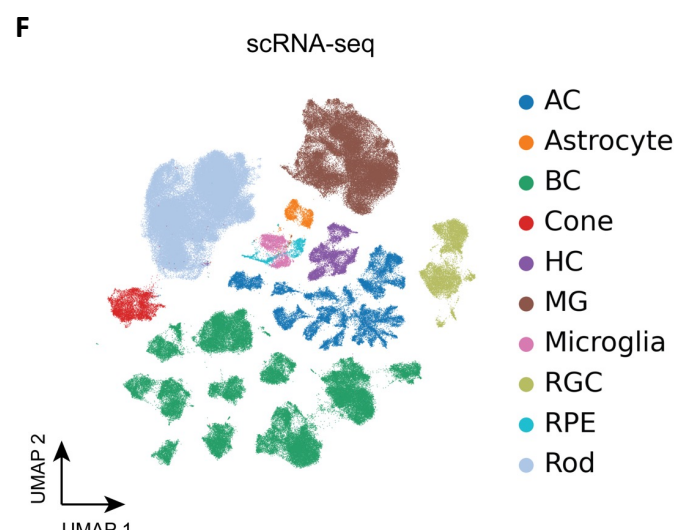
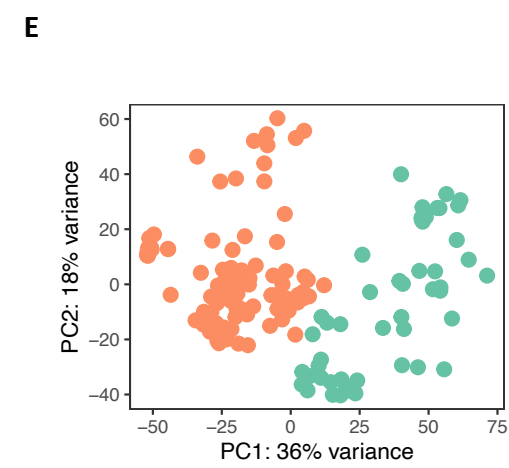
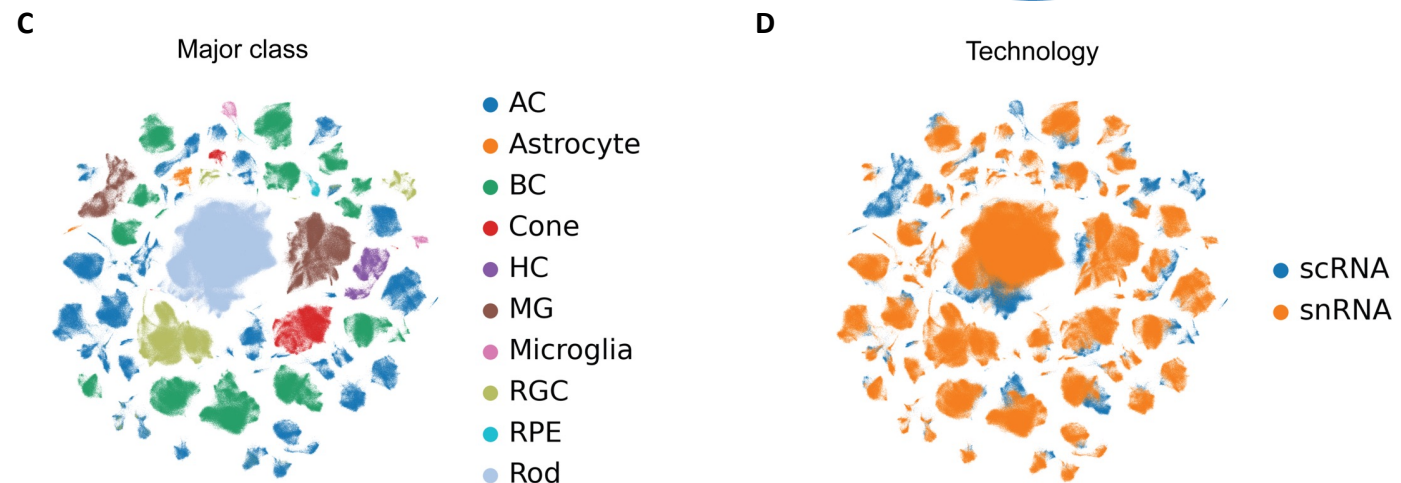
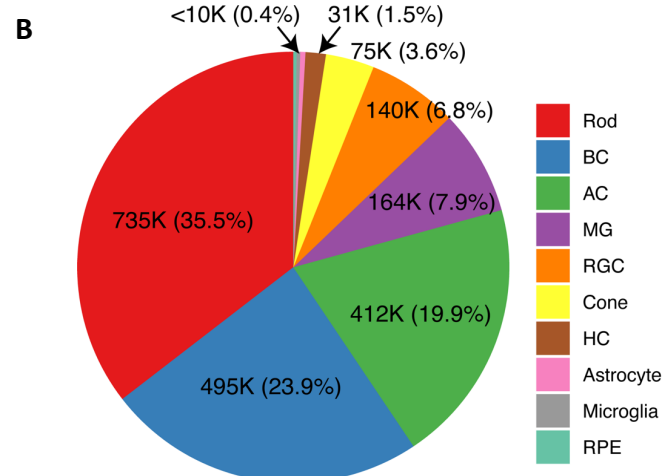
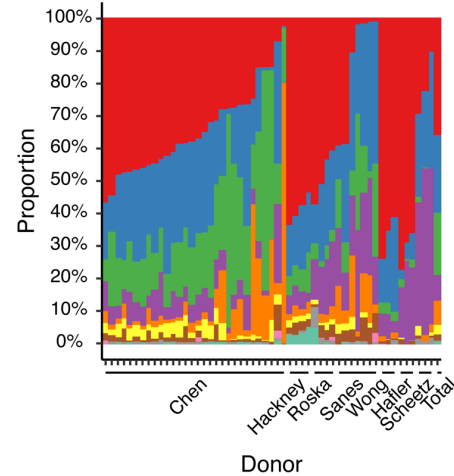
A**B****C****D****Figure 7. Leveraging multi-omics data to study GWAS and eQTL loci**

Figure 7. Leveraging multi-omics data to study GWAS and eQTL loci

A. Cell class enrichment of GWAS loci based on chromatin accessibility with LDSC (left) and gene expression with MAGMA (right). Rows represent enriched GWAS traits, and columns represent retinal cell classes. The highlight dot indicates the enrichment q -value < 0.05 . B. Categorization of fine-mapped GWAS variants located in various genomic regions. Categories include peak (i.e., open chromatin regions), linked cis-regulatory elements (CREs), differentially accessible regions (DARs), promoter, exon, 5_UTR and 3_UTR of gene annotation. C. Categorization of fine-mapped eQTL variants located in various genomic regions. D. Visualization of fine-mapped loci in *CLIC5* region.

Table 1. Summary of fine-mapped GWAS loci associated with the seven GWAS traits.

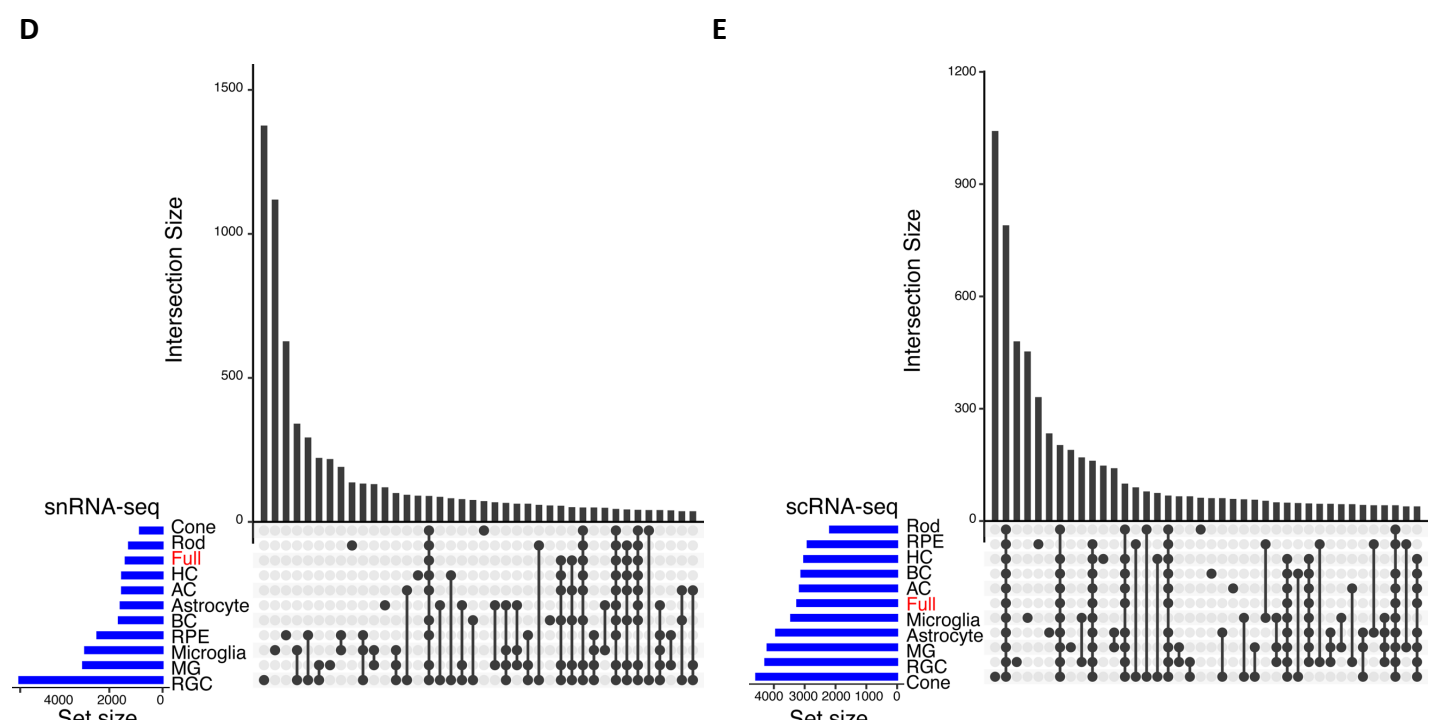
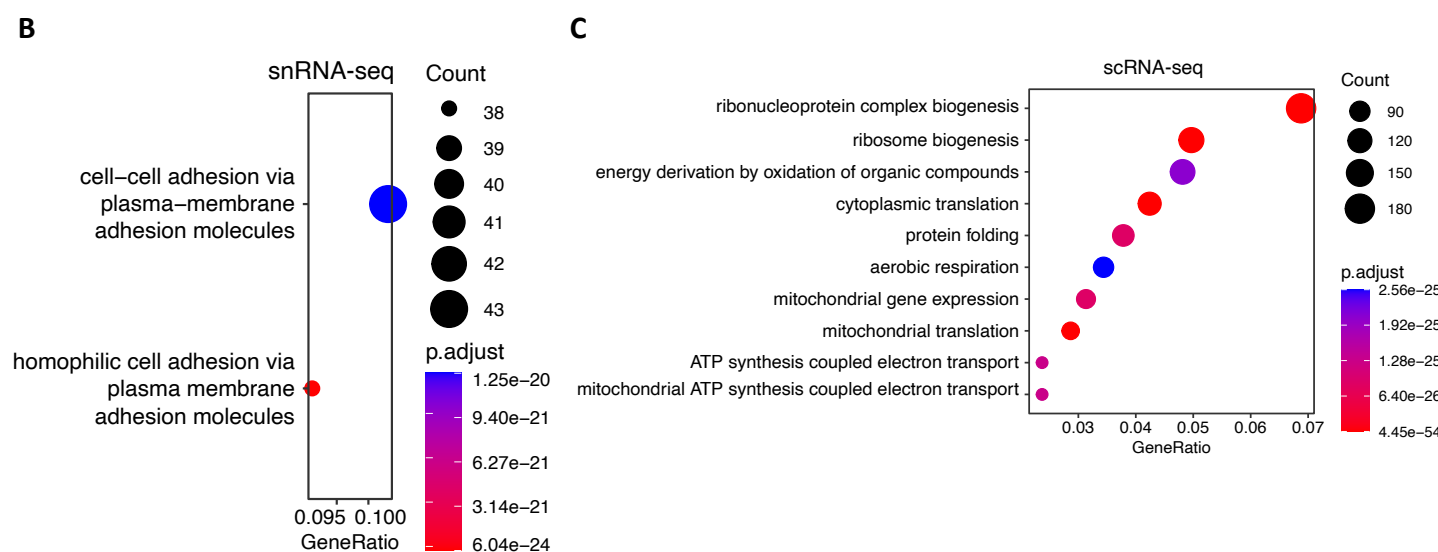
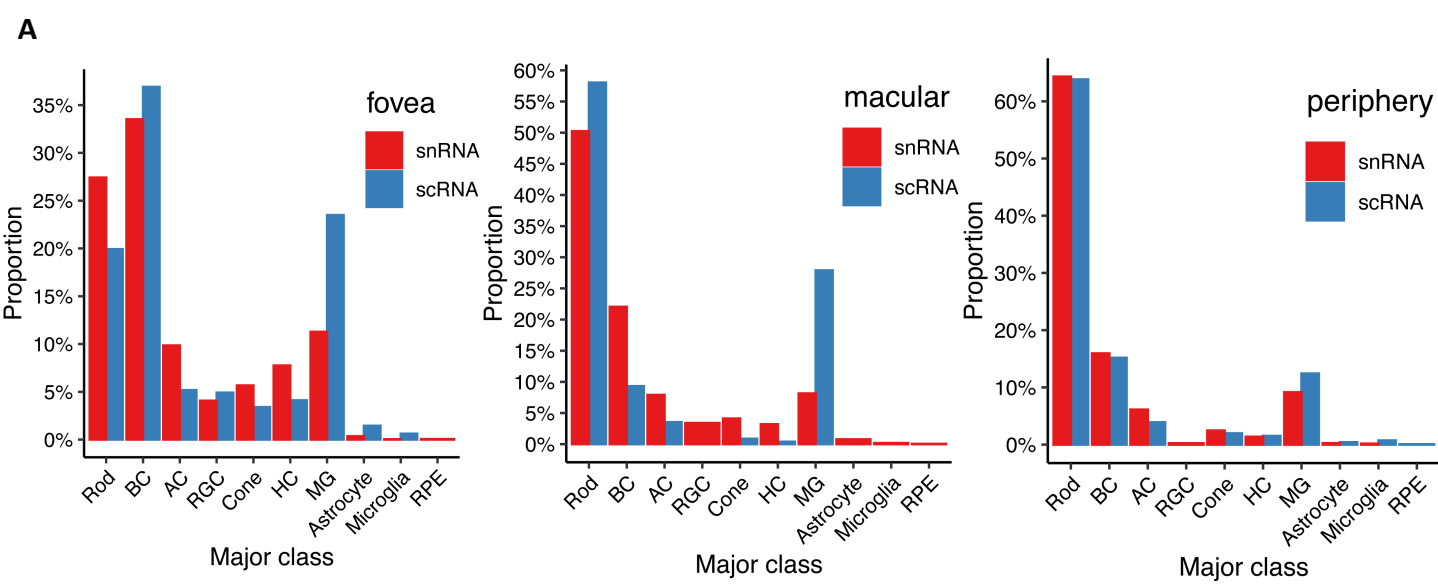
	AMD	Myopia	POAG	Diabetic retinopathy	ONL thickness	IST thickness	OST thickness
Number of fine-mapped genes	56	391	74	3	81	25	61
Overlapped with eQTLs	8	67	11	0	23	8	13
Examples	APOE C2 C3 CRB1 RDH5 TGFBR1	PAX6 PDE6G RDH5 TGFBR1 TOMM40 KCNA4 LHX3	TFAP2B PLEKHA7 EFEMP1 THSD7A TMCO1 CLIC5 SIX6	ABCF1 MIR4640 DDR1	ATOH7 MAPT PAX6 RAX RBP3 RDH5 VSX2	CNGB3 VSX2 RP1L1	MKKS FSCN2 PDE6G PRPH2 RDH5 RHO RP1L1 SAG RLBP1



Extended Data Figure 1. Overview of the HRCA.

Extended Data Figure 1. Overview of the HRCA.

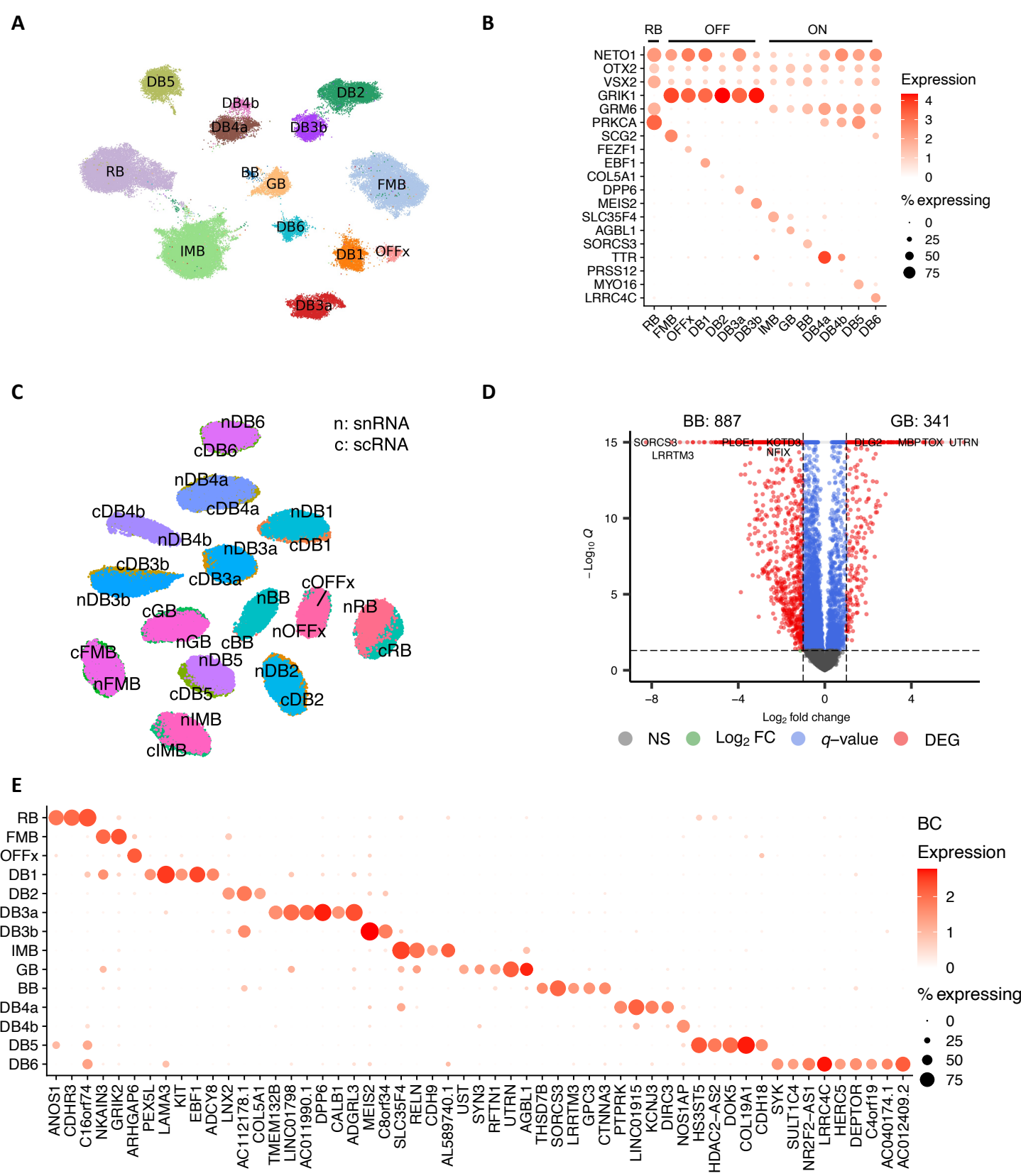
A. Cell proportion distribution of major classes among donors. The x-axis corresponds to each donor, and the y-axis is the cell proportion of major classes. The last bar is the cell proportion across total cells. B. A pie chart illustrating the number of cells for major classes and their proportions. C. Integration of datasets from snRNA-seq and scRNA-seq datasets. The cells are colored by major classes. D. The atlas is colored by the two technologies: snRNA-seq (in coral) and scRNA-seq (in blue). E. The distribution of transcriptomic data for 152 samples obtained from snRNA-seq and scRNA-seq technologies. Each sample is colored by the technology used. F. The atlas of scRNA-seq data, with major classes represented using different colors. G. Dot plots illustrating the distribution of expression levels of marker genes for major cell classes in snRNA-seq (on the left) and scRNA-seq data (on the right).



Extended Data Figure 2. Comparison between single-nuclei and single-cell technologies.

Extended Data Figure 2. Comparison between single-nuclei and single-cell technologies.

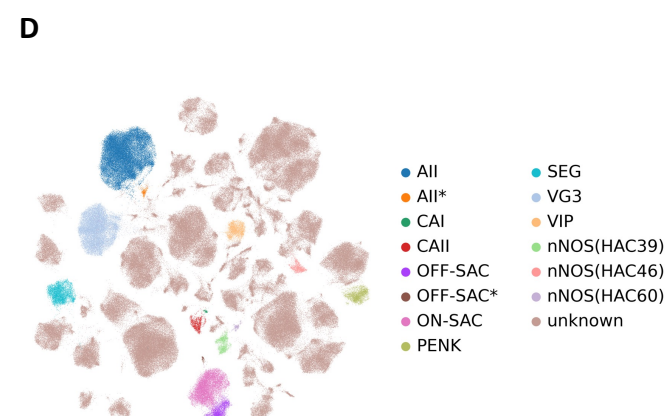
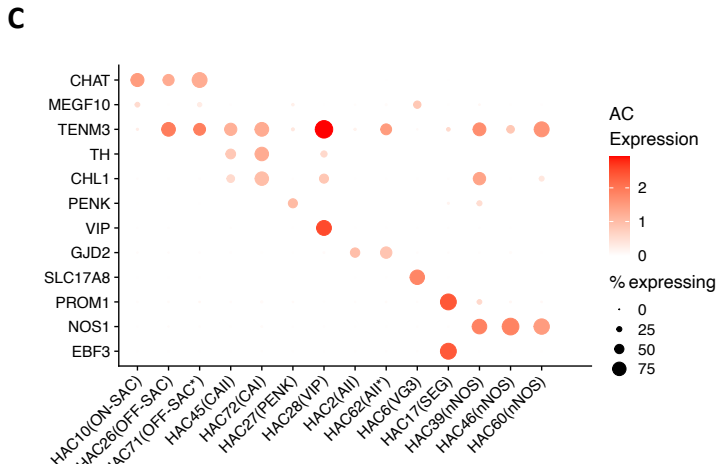
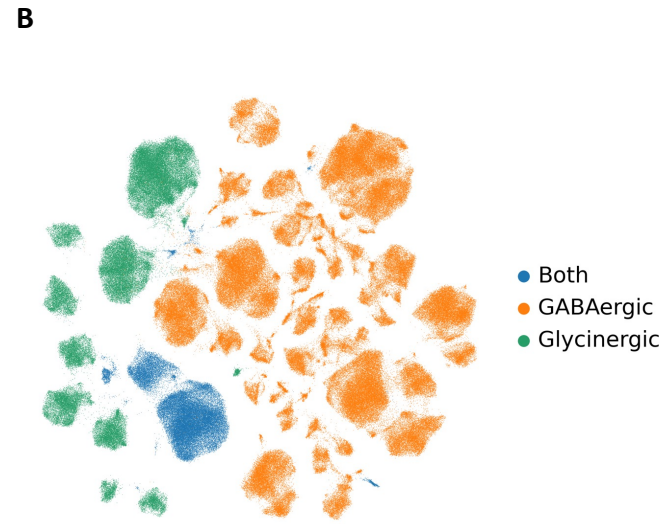
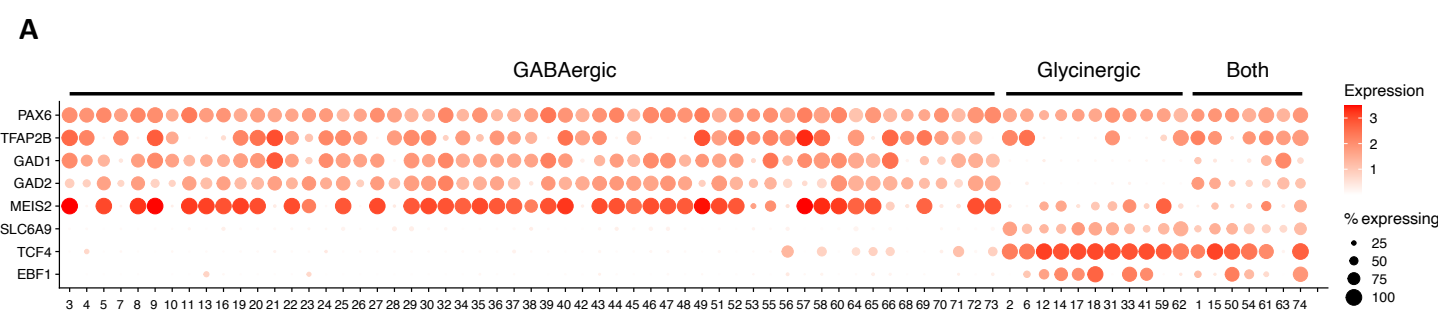
A. Cell proportion of major class of samples between snRNA-seq and scRNA-seq in fovea, macular, and periphery tissue regions. The red bar represents cell proportions of major classes in snRNA-seq samples, and the blue bar represents cell proportions of scRNA-seq samples. B. Enriched GO BPs of 1,387 over-expressed genes in snRNA-seq data. C. Enriched GO BPs of 3,242 over-expressed genes in scRNA-seq data. D. Shared genes over-expressed in snRNA-seq data among major cell classes. The "Full" (in red) is genes over-expressed in snRNA-seq data regardless of cell classes. E. Shared of genes derived from scRNA-seq data.



Extended Data Figure 3. transcriptomic signature of bipolar cells

Extended Data Figure 3. transcriptomic signature of bipolar cells

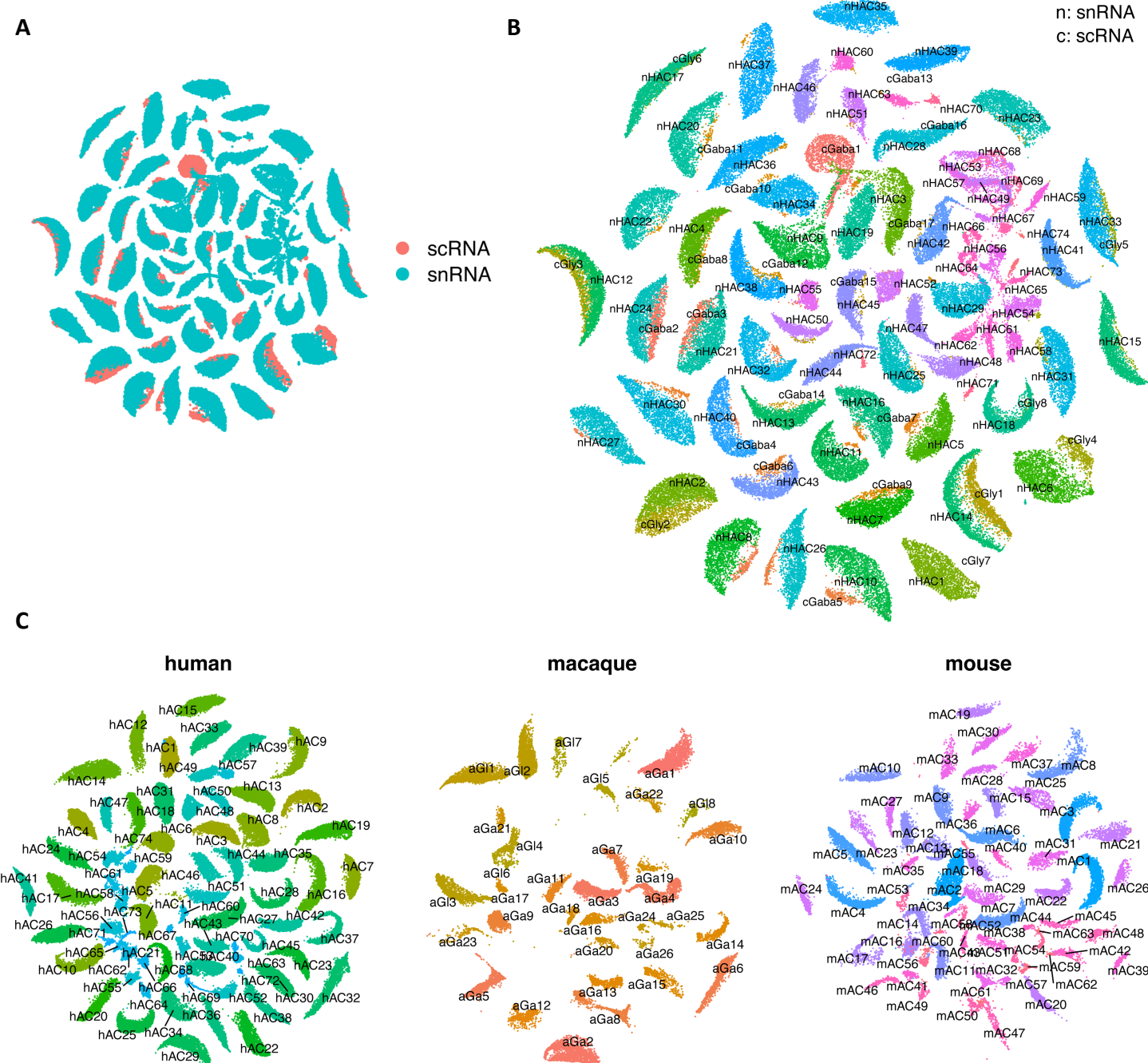
A. UMAP visualization of BC cells based on single-cell transcriptome data. B. Dot plot of the distribution of marker gene expression by the single-cell measurements. C. Co-embedding between snRNA-seq and scRNA-seq cells. The label names are prefixed by “n” for snRNA and “c” for scRNA. D. Volcano plot of differentially expressed genes between GB and BB of the snRNA-seq datasets. Differentially expressed genes were identified under $|\log_2 \text{fold change}| > 1$ and $q\text{-value} < 0.05$. E. Predicted markers per BC cell type by the binary classification analysis using snRNA-seq datasets. Rows are BC cell types, and columns represent novel markers.



Extended Data Figure 4. Annotation of amacrine cells.

Extended Data Figure 4. Annotation of amacrine cells.

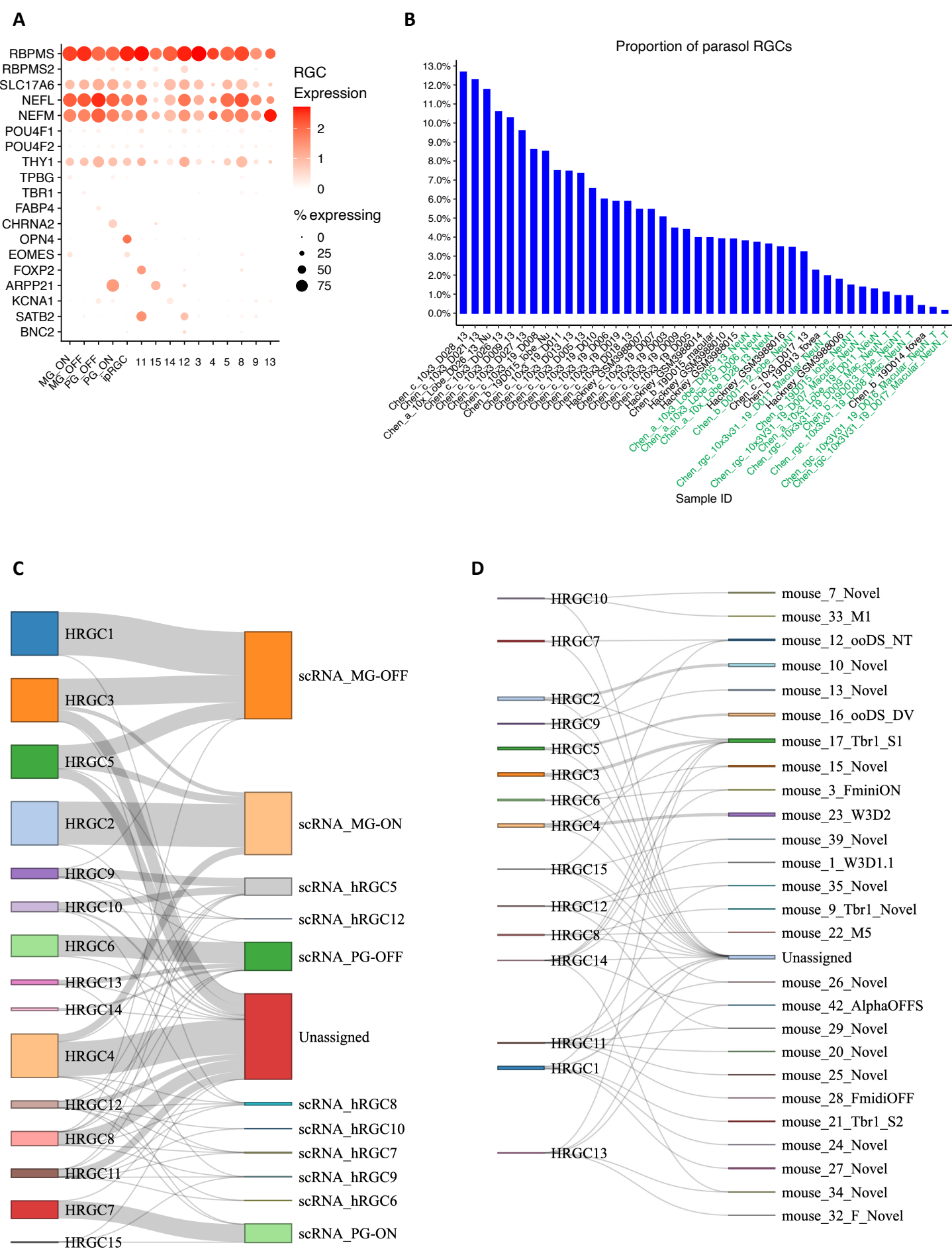
A. Dot plot of AC cell clusters by markers to identify AC subclasses for GABAergic, Glycinergic, and Both. *PAX6* and *TFAP2B* were used as AC pan-markers. *GAD1/GAD2* were used for GABAergic ACs, and *SLC6A9* was used for the Glycinergic ACs. *MEIS2*, *TCF4*, and *EBF1* were also included in the dot plot. B. UMAP of AC cells, colored by the four AC groups. C. Dot plot of 14 AC cell clusters with known markers. The cell type names are indicated in parentheses next to the cluster IDs. D. UMAP visualization of AC cells, colored by the 14 clusters with cell type names. The rest of the clusters are colored as “unknown” without existing names.



Extended Data Figure 5. Cross-mapping for human amacrine cells.

Extended Data Figure 5. Cross-mapping for human amacrine cells.

A. SATURN co-embedding visualization of AC cell types between snRNA-seq and scRNA-seq. AC cells are colored by the two technologies. B. The same SATURN co-embedding with AC type labels color-coded on top of clusters. Labels are prefixed with “n” for snRNA-seq datasets and “c” for scRNA-seq data. C. SATURN co-embedding visualization of AC types across human, macaque and mouse species. AC cell labels for the three species are overlaid on clusters. Labels are prefixed with “h” for human, “a” for macaque, and “m” for mouse.

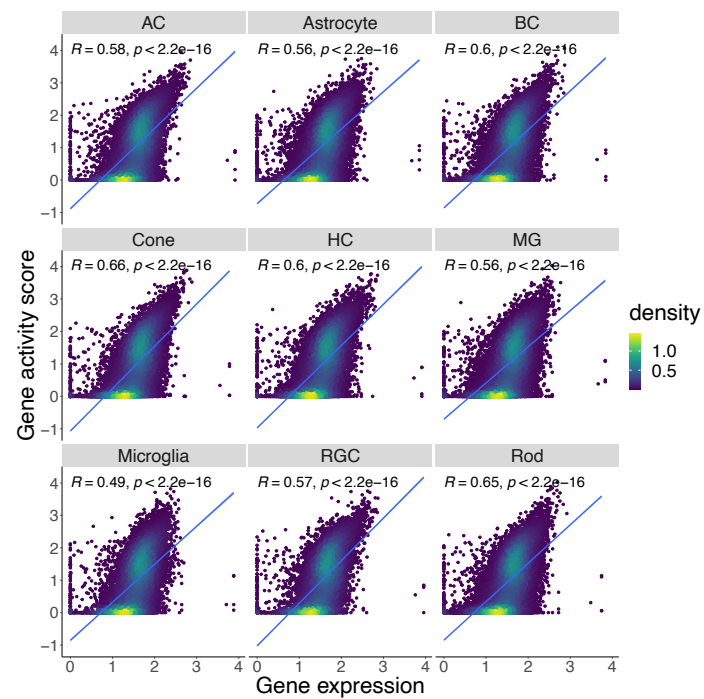


Extended Data Figure 6. Annotation of retinal ganglion cells.

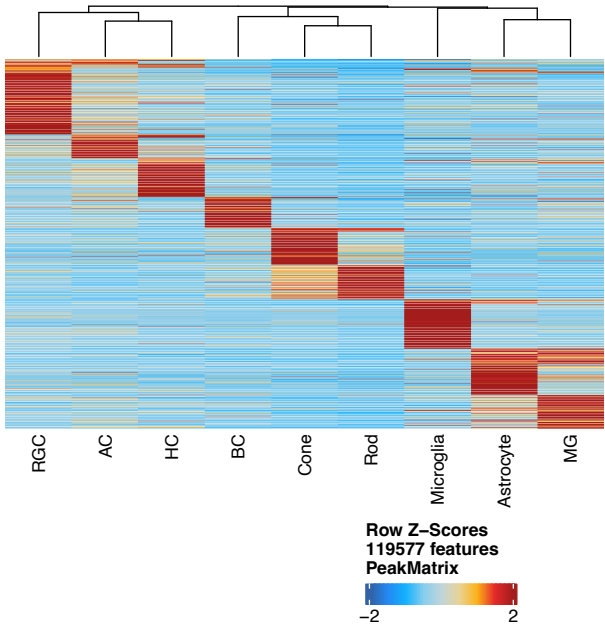
Extended Data Figure 6. Annotation of retinal ganglion cells.

A. Dot plot of RGC cell clusters with existing markers. B. The proportion of parasol RGCs within the RGC population in the samples. Samples enriched by NeuN experiments are highlighted in green. C. Sankey diagram depicting the relationship between RGC clusters from snRNA-seq datasets and the public labeling of RGC types from scRNA-seq datasets. The width of the lines is proportional to the number of cells in the mapping. D. Sankey diagram illustrating RGC types alignment between humans (left column) and mice (right column).

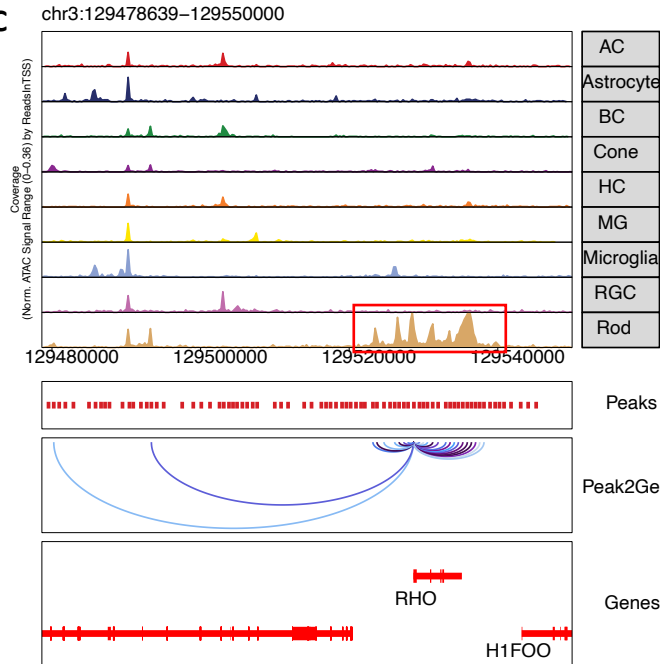
A



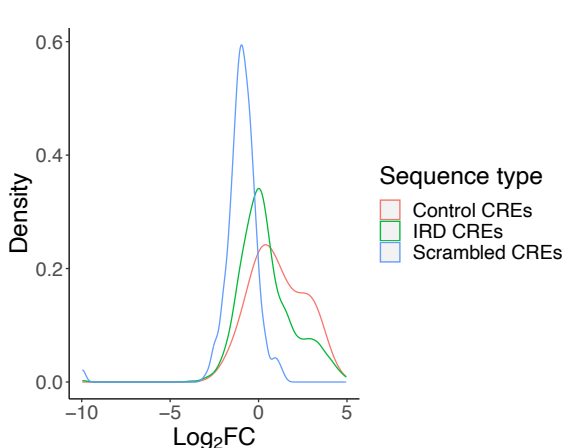
B



C

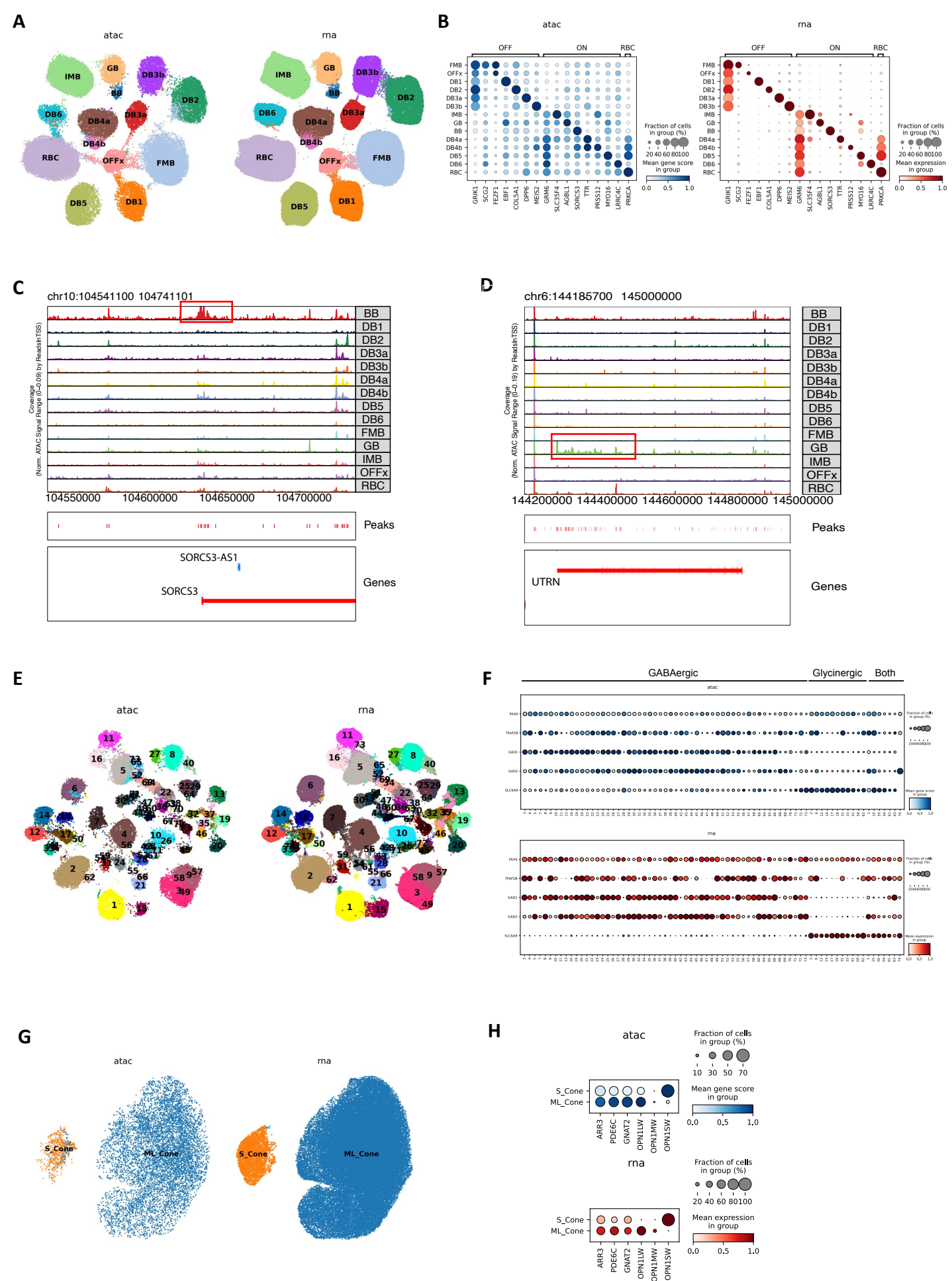


D



Extended Data Figure 7. A high resolution snATAC-seq cell atlas of the human retina

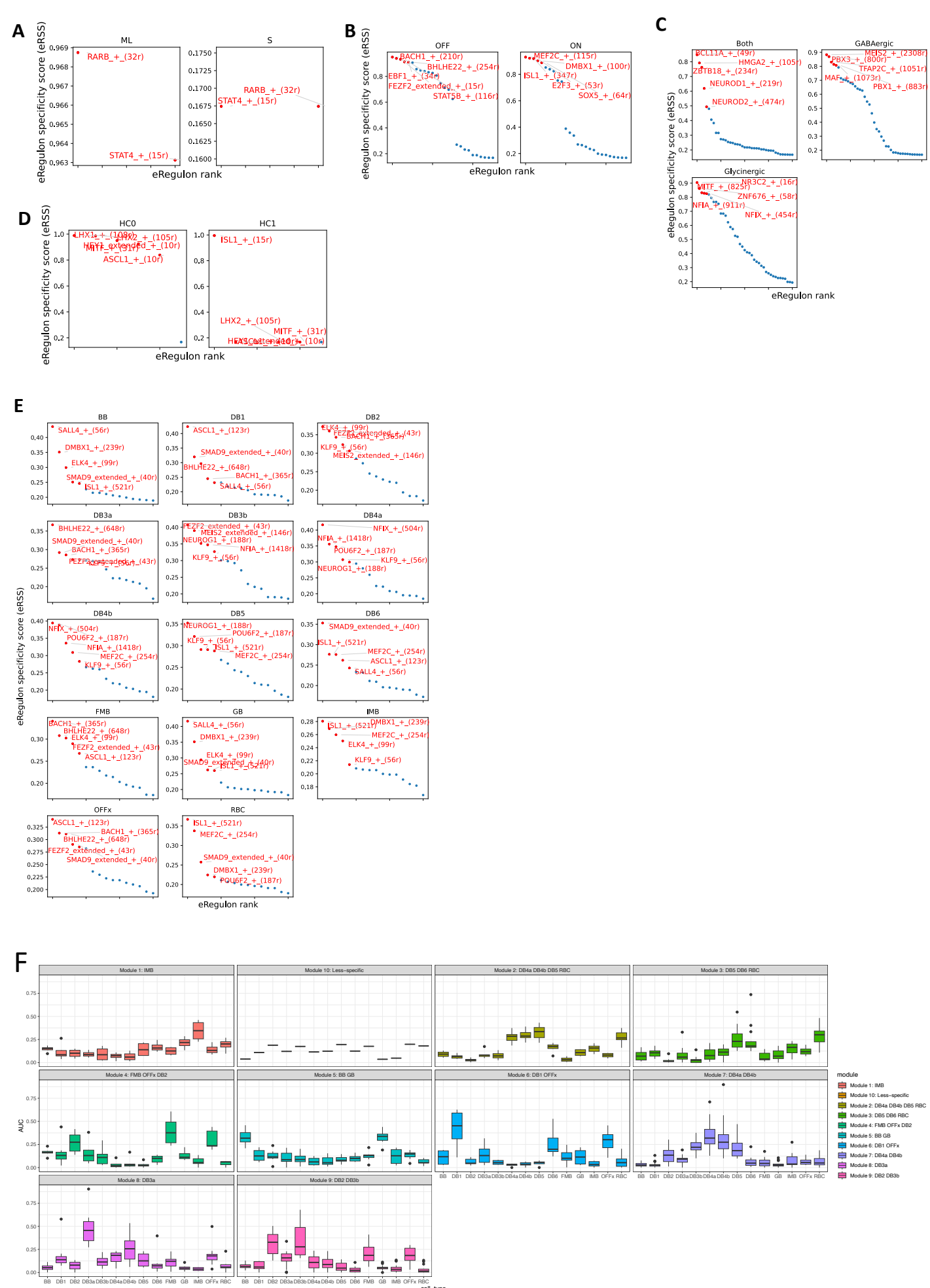
A. Scatter plot showing the correlation between gene expression derived from snRNA-seq (X axis) and gene activity score derived from snATAC-seq (Y axis) from major retinal cell classes. B. Heatmap showing the chromatin accessibility of differential accessible regions (DARs) identified in major retinal cell classes. Rows represented chromatin regions specific to certain major classes, and columns corresponded to major classes. C. Genome track of the *RHO* locus showing the cell type specific chromatin accessibility in the promoter and linked cis-regulatory elements of this gene. D. Density plot showing the activity ($\log_{2}FC$ value of comparison between activity of each tested sequence and the activity of a basal CRX promoter) distribution of the tested sequences by MPRAs. IRD CREs n=1,820 (green), control CREs with a variety of activities n=20 (red), Scrambled CREs n=300 (blue).



Extended Data Figure 8. Multi-omics atlas of the human retinal subclass cell types

Extended Data Figure 8. Multi-omics atlas of the human retinal subclass cell types

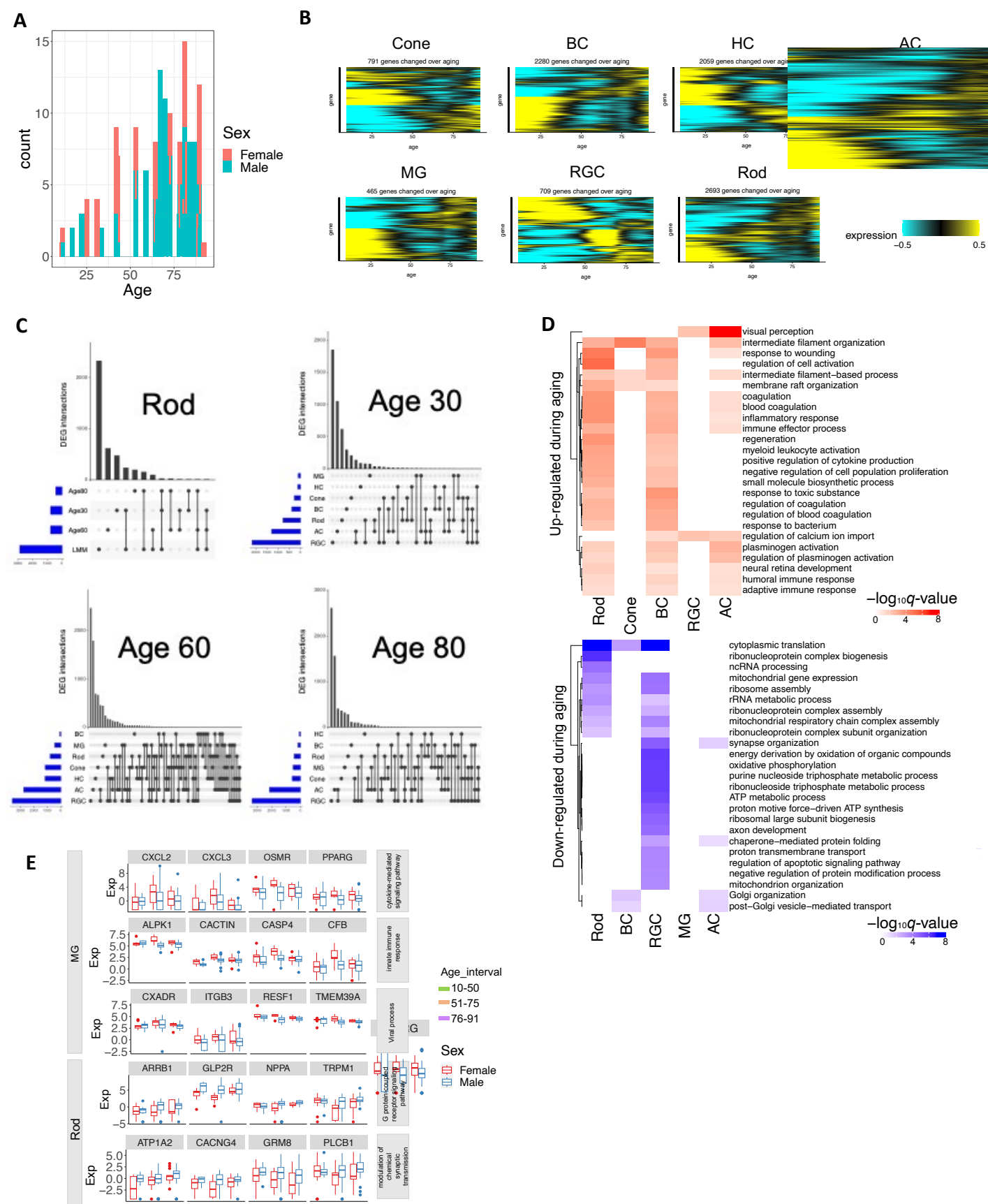
A. UMAP showing the co-embedding of bipolar cells (BC) from snRNA-seq and snATAC-seq were clustered into BC cell types. B. Dot plot showing marker gene expression measured by snRNA-seq and marker gene activity score derived from snATAC-seq are specific in the corresponding BC cell types. C. Genome track of SORCS3 showing the promoter of SORCS3 is specifically open in BB. D. Genome track of UTRN showing the local chromatin of UTRN is specifically open in GB. E. UMAP showing the co-embedding of amacrine cells (AC) from snRNA-seq and snATAC-seq were clustered into AC cell types. F. Dot plot showing marker gene expression measured by snRNA-seq and marker gene activity score derived from snATAC-seq are specific in the corresponding sub classes of AC types. G. UMAP showing the co-embedding of cone cells (Cone) from snRNA-seq and snATAC-seq were clustered in Cone cell types. H. Dot plot showing marker gene expression measured by snRNA-seq and marker gene activity score derived from snATAC-seq are specific in the corresponding Cone cell types.



Extended Data Figure 9. Regulon of the human retinal subclass cell types

Extended Data Figure 9. Regulon of the human retinal subclass cell types

A. Dot plot showing the distribution of regulon specificity score of regulons identified in ML- and S-Cone. B. Dot plot showing the distribution of regulon specificity score of regulons identified in OFF- and ON-BC (ON-BC include ON-Cone BC and Rod BC). C. Dot plot showing the distribution of regulon specificity score of regulons identified in GABAergic-, Glycinergic- and Both-AC. D. Dot plot showing the distribution of regulon specificity score of regulons identified in HC0 and HC1. E. Dot plot showing the distribution of regulon specificity score of regulons identified in 14 BC cell types. F. Boxplot showing the average AUC values of the regulon modules identified in BC cell types. The BC cell types with the highest AUC values were labeled in the title of each regulon module.



Extended Data Figure 10. Differential gene expression during aging and associated with sex.

Extended Data Figure 10. Differential gene expression during aging and associated with sex.

A. Age and sex distribution of the analyzed samples. B. Heatmap showing gene expression level of differentially expressed genes (DEGs) during aging in major retinal cell classes identified with linear mixed effect model (LMM). C. UpSet plot showing the overlap of DEGs identified by LMM and sliding-window analysis at the age of 30, 60 and 80 in Rod. UpSet plot showing the number of DEGs across major retinal cell classes at the age of 30, 60 and 80, respectively. D. The GO terms significantly enriched (FDR <0.1) of DEGs during aging identified by LMM across retinal cell classes. E. The examples of DEGs between male and female associated with the enriched GO terms.